ICFO Institut de Ciències Fotòniques

Universitat de Barcelona

UAB Universitat Autònoma de Barcelona

UPC Universitat Politècnica de Catalunya BarcelonaTech

Master in Quantum Science and Technology

A laser system for cooling strontium atoms in a new Rydberg atom-array experiment

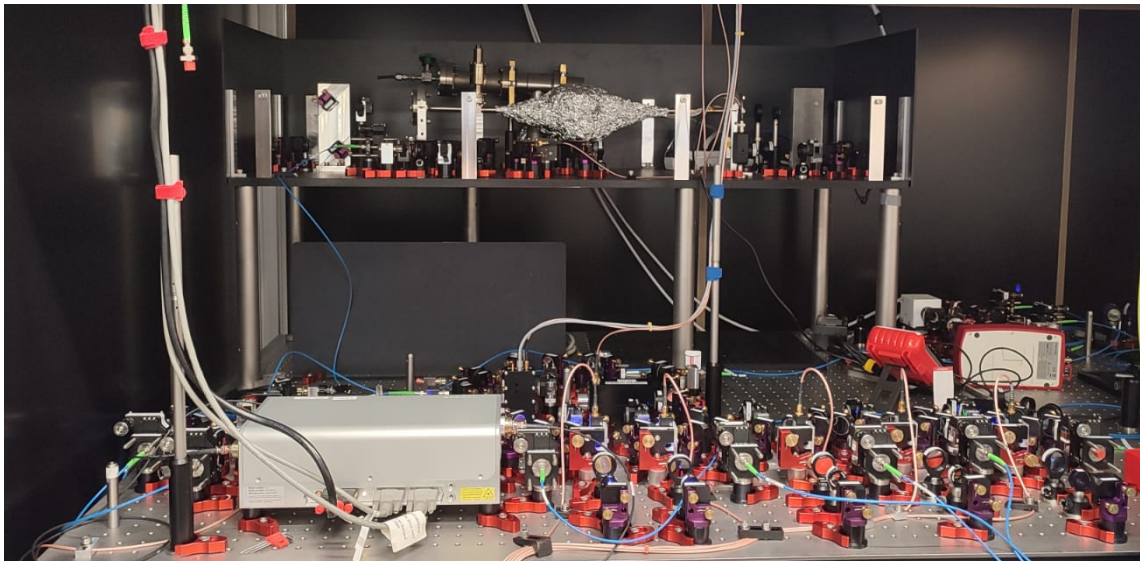

Irene Prieto Rodríguez

Supervised by Prof. Dr. Leticia Tarruell

2023-2024

A laser system for cooling strontium atoms in a new Rydberg atom-array experiment

Irene Prieto Rodríguez

Supervised by: Prof. Dr. Leticia Tarruell

ICFO, Mediterranean Technology Park, Avinguda Carl Friedrich Gauss, 3, 08860 Castelldefels, Barcelona
August 2024

In this work we report on the construction of a laser system for laser cooling of strontium atoms. This lays the foundation to a new cold atoms experiment which aims to simulate lattice gauge theories with Rydberg decorated tweezer arrays. The developed laser system uses the $^1S_0 \leftrightarrow {}^1P_1$ transition of strontium-88 at 461 nm. We focus on the master laser frequency stabilisation through an active spectroscopic feedback on a vapour cell. Therein, the high vacuum regime has been restored and new strontium has been introduced as part of this thesis project. We explore Doppler-free spectroscopy through saturated absorption, specifically locking the master laser on a modulation transfer spectroscopy signal. In addition, we address the need for specific frequency control in the different cooling stages of the experiment by implementing the use of acousto-optical modulators. Finally, we tackle the required optical power amplification by assembling and characterising one of the slave lasers that will be used to that end, ensuring thereby the suitability of the laser system for its purpose.

Keywords: Cold atoms, laser system, strontium, Doppler-free spectroscopy, acousto-optical modulator, slave laser

Irene Prieto Rodríguez: ireneprietorodriguez@gmail.com

Acknowledgements

Working in the ultracold quantum gases group at ICFO over the past months has been a wonderful experience, and I would like to express my gratitude to everyone who made this possible.

First and foremost, I want to thank Leticia for giving me the opportunity to delve into the fascinating field of cold atoms, and for entrusting me with the task of building the blue laser system for the new Rydberg experiment. Thank you for your valuable guidance, your commitment and determination, and for fostering an excellent working atmosphere within the team.

I am especially grateful to Ana and Jonatan for their supervision and guidance in the lab throughout this project. Thank you for willingness to help, for taking the time to answer all my questions, and for your exceptional advice. Working with you has been an absolute pleasure, and I will always be grateful for everything you have taught me. This work would not have been possible without your support.

I would also like to express my gratitude to Roxana for being a great teammate during the last months of my thesis. Your positive energy in the lab, your essential assistance with the last measurements, and your valuable suggestions during the revision of this report have been greatly appreciated. I have no doubt that you will do an excellent work finalising the laser system with the slaves setup!

Moreover, I want to thank the other members of the Rydberg team: Théo, for his kindness and impressive work building the optical tweezers setup; and Sara, for being such a nice desk neighbour, and for her fundamental work on the Rydberg coils.

In addition, I want to thank Toni for his invaluable help with the heat pipe, always finding the time to assist Ana and me with the vacuum procedures. Battling the strontium block and getting the spectroscopy signal would have been impossible without you!

A big thank you to all the fellow master's students in the team—Lucía, Judith and José. Sharing this experience with you has been wonderful.

Furthermore, I want to extend my gratitude to the entire QGE team for being so welcoming, helpful and kind. Thank you for the interesting physics discussions, for making lunch time so enjoyable, and for offering great advice during a year filled with tough decisions about the future. I am truly grateful to have met all of you.

To conclude, I want to thank my friends and family for their endless love and support, for always believing in me, and for making my life so much happier.

Contents

1 Introduction

The study of interacting many-body quantum systems is a very challenging task. The size of the associated Hilbert space grows exponentially with the number of particles involved, and simply considering one particular configuration—as one could do in classical mechanics—is not possible, due to one of the fundamental postulates laying at the core of quantum mechanics: the superposition principle. Hence, numerical calculations on the dynamics of these complex systems are restricted to a small number of components, even for the most powerful existing supercomputers. Overcoming the limitations of classical computing resources is key to address open questions in diverse areas of physics.

This problem was already outlined by Richard P. Feynmann back in 1982, when he stated the precursory idea of using quantum systems, instead of classical computers, to simulate quantum mechanics, sowing the seeds of quantum simulation [1]. This seminal idea has led to two distinct approaches for surpassing classical computing limitations: analogue and digital quantum simulation. The pivotal difference between them is whether the defining physical parameters are continuous or discrete, respectively. This debate is not new either, it did also happen in the scope of classical simulators. Therein, digital simulators—classical computers— have doubtlessly prevailed over analogue options, but this has only been possible after the development of adequate hardware technologies. Over centuries, both routes coexisted and analogue machines (e.g. the Antikythera mechanism and the astrolabe in the context of the study of the cosmos, or the differential analyser for solving differential equations) played an essential role by providing answers to specific problems when digital computers were not ready yet to do so. Likewise, today we do not have yet the required technology for exploiting the full potential of digital quantum computation, and the so-called quantum advantage is yet to be reached. However, practical quantum advantage is already available through special-purpose analogue simulators [2]. This strategy consists on mapping the Hamiltonian of interest into a highly controllable quantum system, conveniently preparing initial states that are physically relevant, and finally performing reliable high-precision measurements on the simulator [3]. This scheme does not only provide deep insights into the underlying physics of the targeted system, but it also gives access to new physical regimes that are unavailable in the natural counterpart.

There is a wide variety of platforms on which analogue and digital quantum simulations are performed nowadays. Key examples are ultracold neutral atoms in the continuum [3], in optical lattices [4], and arrays of neutral atoms excited to Rydberg states [5], trapped ions [6], ultracold molecules [7], superconducting circuits [8], quantum dots [9] or photonic circuits [10]. Each of these platforms has specific technical advantages and disadvantages, making them suitable for particular purposes. In the present work, we will focus on neutral atoms, which have allowed for historical breakthroughs, such as the first experimental realisation of Bose-Einstein condensates [11], and Fermi degenerate gases [12]. Laser cooling and manipulation techniques developed through the last decades allow for a great control and tunability of the platform, allowing for interaction control using Feshbach resonances [13], single-atom detection in quantum gas microscopes [14], and generating arbitrary geometrical arrangements using optical tweezers [15].

One of the many aspects in which engineered quantum systems offer the prospect of sidestepping the limitations of conventional computation methods is the study of gauge theories [16, 17]. They play a fundamental role in our understanding of nature, encompassing a wide range of areas in physics, from the fundamental interactions between elementary particles in the context of high-energy physics [18], to low-energy effective descriptions of strongly correlated systems in condensed matter [19]. Therein, gauge theories provide

insights into a plethora of fascinating phenomena, such as high temperature superconductivity [20], fractional quantum Hall effect [21] or quantum spin liquids [22]. In the last years, there has been an immense effort to implement gauge theories on engineered quantum devices. This is an extremely challenging task, precisely due to the local conservation laws that characterise gauge theories, and whose experimental implementation is far from trivial. In 2016, the first experimental demonstration of the digital quantum simulation of a gauge theory was achieved on a system of four trapped ions, successfully realising the Schwinger model, which is a 1+1-dimensional lattice gauge theory (LGT) describing quantum electrodynamics [23]. LGTs emerge when a gauge theory is studied under a discretisation of space-time, simplifying it as a lattice with matter particles on its sites and gauge fields on the links between them. We talk about a 1+1-dimensional LGT referring to a single spatial dimension, and the temporal one. Implementations of the Schwinger model based on trapped ions architectures have been improved over the years [24, 25], and similar models have been implemented with arrays of Rydberg atoms as well, which allow for larger system sizes [26, 27]. In addition, the aforementioned Schwinger model has also been studied with arrays of bosonic atoms in optical superlattices [28, 29]. Moreover, a topological gauge theory, in particular a one-dimensional reduction of the Chern Simons theory of fractional quantum Hall states, has been realised in a Bose-Einstein condensate [30], precisely in the group in which this master thesis has been conducted.

These impressive pioneering experimental achievements have paved the way for the quantum simulation of gauge theories, but they all remain constrained to one spatial dimension. The natural next step in the ongoing seek for exploring the rich physics of gauge theories is to engineer higher dimensional implementations in the lab. Key building blocks, based on Floquet engineering in an optical lattice [31], or using interspecies spin-changing collisions in an atomic mixture [32], have already been successfully demonstrated. The ultracold quantum gases group at ICFO aims to address this problem with a new approach. This is the challenging long term goal of the new experiment that we are currently building. To this end, arrays of strontium atoms trapped with optical tweezers and excited to Rydberg states will be utilised. As in any other ultracold neutral atoms experiment, the initial step is to reach near absolute zero temperatures. This requires a laser system providing all the necessary light beams, each with specific frequency and power. This thesis focuses on the construction and frequency stabilisation of a laser system based on the 461 nm transition of strontium, which will be used in the initial stages of the cooling and trapping strategy, and for imaging purposes.

The rest of the thesis is organised as follows. In Sec. 2 we review some of the principles of laser cooling and trapping, which will be used throughout this work. The key features of the new experiment in which this thesis is framed are presented in Sec. 3. Section 4 is devoted to the laser system, focussing on its frequency stabilisation through absorption spectroscopy, the use of acousto-optical modulators to implement controlled frequency shifts, and briefly discussing its power amplification through slave lasers. Finally, we summarise the project and its outlook in Sec. 5.

2 Laser cooling and trapping

In this section, we review some of the principles on which numerous standard techniques in the field of ultracold atoms are based. We aim to study the interaction of an atomic cloud with a laser beam whose frequency is nearly resonant with a given atomic transition. For the sake of simplicity, we only consider the two atomic levels involved in the transition of interest, whose frequency is denoted as ω_0. A photon with a frequency ω will be absorbed

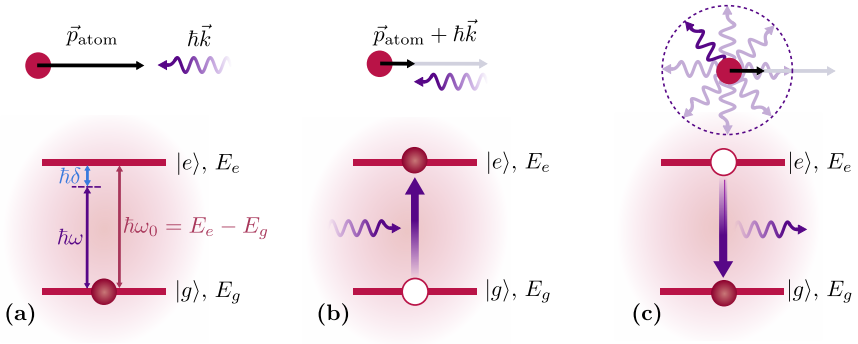

Figure 1: Principle of laser cooling. **(a)** A two-level atom in the ground state $|g\rangle$ and momentum $\vec{p}_{\text{atom}}$ interacts with a counter-propagating photon with momentum $\hbar\vec{k}$, and frequency ω, which is almost resonant with the atomic transition.**(b)** The photon is absorbed by the atom, transferring its momentum and energy to it. Therefore, the atom is raised to the excited state $|e\rangle$. **(c)** A new photon is spontaneously emitted by the atom, which goes back to the ground state.

by an atom initially in the ground state, exciting it, with a probability given by a Lorentzian distribution,

$$L(\delta;\Gamma) \equiv \frac{\Gamma/(2\pi)}{\delta^2 + (\Gamma/2)^2}, \tag{1}$$

where Γ is the natural linewidth of the transition, and $\delta \equiv \omega - \omega_0$ is the frequency detuning. This absorption process also implies that the photon momentum, given by $\vec{p}_\nu = \hbar\vec{k}$ (where $\vec{k}$ is the photon wavevector), is transferred to the atom. Subsequently, the excited atom will decay through spontaneous emission to the ground state after an average time of $1/\Gamma$. Let us emphasise that the probability of emitting a photon in a given direction or in the opposite one are equal, so the direction of the emitted photon is random. Hence, on average, the atom recoil after spontaneous emission does not have a net effect on the atom momentum. Nevertheless, there is a total momentum transfer from the light field to the atom during absorption. Therefore, this process yields a *radiation force* given by

$$\vec{F}_{\vec{k}}\,(\delta;\Gamma) = \frac{\Gamma}{2}\,\frac{s_0}{1 + s_0 + (2\delta/\Gamma)^2}\hbar\vec{k}, \tag{2}$$

where s_0 is the saturation parameter defined as $s_0 \equiv I/I_{\text{sat}}$, where I is the light intensity and $I_{\text{sat}} = (\hbar\omega^3\Gamma)/(12\pi c^2)$ is the saturation intensity [33]. The described process is depicted in Fig. 1.

Let us extend the above described model, and consider that our atom is moving with velocity $\vec{v}$. The radiation frequency perceived in the atom's frame of reference includes a Doppler shift given by $\omega_D = -\vec{k}\cdot\vec{v}$. Hence, Eq. (2) needs to be rewritten replacing δ by the effective detuning, which reads $\delta_{\text{eff}} \equiv \delta - \vec{k}\cdot\vec{v}$.

Remarkably, the Doppler effect can be used to cool down an atomic cloud by superimposing two counter-propagating laser beams of the same frequency (see left panel in Fig. 2). This results in a force in the direction of the light beams given by

$$F(\delta,\vec{v};\Gamma) \equiv \frac{\Gamma\hbar k}{2}\left[\frac{s_0}{1 + s_0 + 4(\delta - \vec{k}\cdot\vec{v})^2/\Gamma^2} - \frac{s_0}{1 + s_0 + 4(\delta + \vec{k}\cdot\vec{v})^2/\Gamma^2}\right]. \tag{3}$$

Let us denote the atom velocity component in the direction of the light beam as v (naturally, it will only coincide with the vector magnitude if $\vec{v} \parallel \vec{k}$). It is straightforward to obtain the first terms in the Taylor expansion of the force F around $v = 0$,

$$F(\delta, v;\Gamma) = \frac{s_0}{[1 + s_0 + (2\delta/\Gamma)^2]^2}\,\frac{8\,\hbar k^2\delta}{\Gamma}\,v + O\left(v^2\right). \tag{4}$$

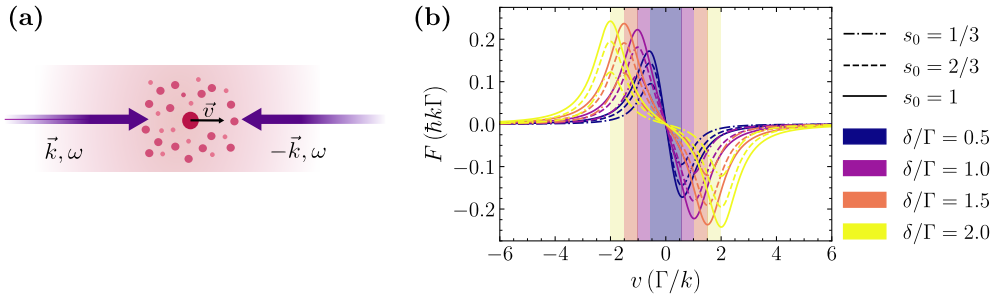

Figure 2: Doppler cooling. **(a)** An atom with velocity $\vec{v}$ interacts with two counter-propagating laser beams of the same frequency ω. **(b)** Doppler cooling force, given by Eq. (3) as a function of the atom's velocity component in the beams direction, v, for different values of δ/Γ and s_0. The cooling velocity range for each ratio δ/Γ is highlighted with the corresponding lighter color.

The zero-order term vanishes, and the force is approximately proportional to the atom velocity component v. In the case of red-detuned light ($\delta < 0$), the direction of this force is opposite to the atom velocity, acting as a viscous damping, and slowing down the atomic cloud in the $\vec{k}$ direction. The force as a function of v is represented on the right panel in Fig. 2 for different values of the saturation parameter s_0, and the ratio δ/Γ. The highlighted areas denote the cooling regions, in which the slope of the force around $v = 0$ is negative and the atoms are slowed down. For fixed values of δ, s_0 and k, we observe that wider transitions lead to a larger cooling range of velocities. However, there is an important drawback associated with Doppler cooling on transitions with a large linewidth, as we explain in the following. Although the momentum exchange between the atoms and the spontaneously emitted photons does not lead to a net force, these momentum kicks result in a random walk in momentum space, heating up the atoms by increasing the velocity variance. This effect limits the range of temperatures that can be accessed through Doppler cooling, leading to a minimum value, known as *Doppler temperature*, which is proportional to the natural linewidth of the transition,

$$T_D = \frac{\hbar\Gamma}{2k_B}. \tag{5}$$

For the above-described deceleration process to be efficient, the resonance condition ($\delta_{\text{eff}} = \delta - \vec{k}\cdot\vec{v}$) must be approximately fulfilled. Nevertheless, the velocity changes bring the atoms out of resonance due to the Doppler effect. This will be a problem if one attempts to slow down an atomic beam with a counter-propagating laser beam. However, it is possible to compensate for the Doppler shift by introducing a conveniently taylored magnetic field. This scheme is known as *Zeeman slower*.

In the absence of a magnetic field, the atomic fine-structure sub-levels m_J are degenerate, but this degeneracy is removed if a weak magnetic field is included. This is caused by the Zeeman effect, which is responsible for the splitting of these degenerate sub-levels. It produces an additional term in the effective detuning, the so-called *Zeeman shift*, given by

$$\delta_Z \equiv \frac{\mu_B}{\hbar}(g'_J m'_J - g_J m_J)B \quad \Rightarrow \quad \delta_{\text{eff}} = \delta - \vec{k}\cdot\vec{v} - \delta_Z, \tag{6}$$

where μ_B is the Bohr magneton, g_J and m_J (g'_J and m'_J) are the Landé g-factor and the total angular momentum projection of the ground (excited) state, respectively. In this equation, $B = B(\vec{r})$ is the magnetic field on the quantisation direction of the total angular momentum J.

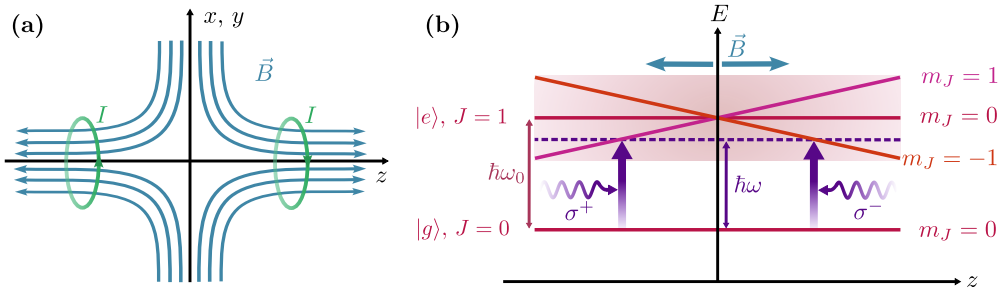

Figure 3: Principle of a MOT in one dimension. **(a)** A quadrupole magnetic field produced by a pair of coils with opposite currents. In this configuration, there is rotational symmetry around the z axis, so the vertical direction can be given by any vector in the XY-plane. A quadrupole field can also be obtained with four identical magnets. Indeed, this is the chosen approach for the 2D MOT of the experiment to which this master thesis is devoted. **(b)** One-dimensional MOT scheme. The spatial dependence of the energy levels in the surroundings of the trap centre, as well as the light-induced transitions, are displayed.

Furthermore, the Zeeman effect can be exploited to trap an atomic cloud with a *magneto-optical trap* (MOT). Similarly to the Zeeman slower, it also utilises an inhomogeneous magnetic field, which creates a spatial dependence in the radiation force. The working principle of a MOT is illustrated in Fig. 3, in the paradigmatic case of a two-level atom immersed in a quadrupole magnetic field, with angular momentum $J = 0$ in the ground state and $J = 1$ in the excited state—which is precisely the situation of the $^1\mathrm{S}_0 \leftrightarrow {}^1\mathrm{P}_1$ transition of strontium, on which the laser system developped in this thesis is based. At the centre of the trap, the magnetic field is null, and it can be approximated as linear in the central region. Let us consider an atom with zero nuclear spin, and therefore no hyperfine structure—again, this corresponds exactly to the case of our laser system for bosonic strontium. Hence, the Zeeman shift also varies linearly with position for each $J = 1$ fine atomic sub-level, as shown in panel (b). Quantum selection rules only allow for transitions in which $\Delta m_J = \pm 1$. This is experimentally realised with circular polarised light $\sigma^{\pm}$, which drives the transitions $m_J \to m_J \pm 1$, respectively. A MOT in one dimension requires two counter-propagating beams of the same frequency, with opposite circular polarisations, as depicted in the scheme. For an atom in the $z > 0$ region, the sub-level $\Delta m_J = -1$ becomes resonant, and the transition from the ground state $m_J \to m_J - 1$ can be driven by the σ^- light beam, which exerts a radiation force that sends the atom towards the centre of the trap. Analogously, atoms in the $z < 0$ region absorb light from the counter-propagating σ^+ beam, which pushes them to the opposite direction, also towards the trap center. It is straightforward to extend this technique to higher dimensions: one simply needs to replicate the described scheme in each direction. Thus, 2D and 3D MOTs are widely employed in ultracold atoms experiments.

All the techniques discussed in this section are planned to be used in the new experiment in which this master thesis is framed. An overview of its main features is provided in the following section.

3 A Rydberg atom array experiment

3.1 Proposal for simulating lattice gauge theories

As we outlined in the introduction, the study of gauge theories is fundamental for improving our understanding of nature, but it is also extremely challenging. Multiple quantum platforms have been used to explore the Schwinger model, which describes electromagnetism in a discretised, one-dimensional space. Unfortunately, the experimental realisation of higher

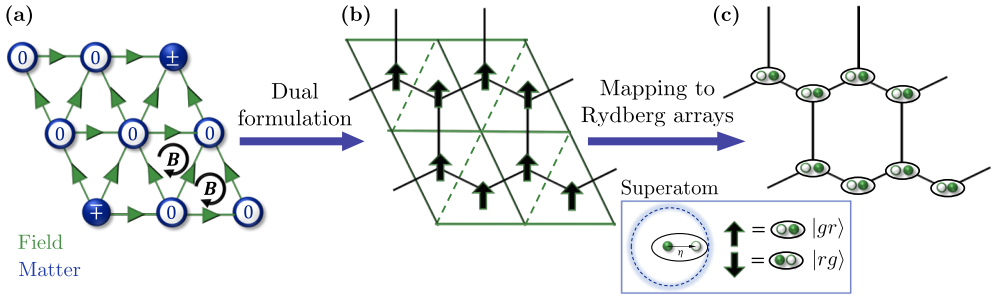

Figure 4: Simulation proposal. **(a)** 2D LGT describing electromagnetism on a triangular lattice. The blue circles represent matter (i.e. charges), and the links connecting them, shown as green arrows, encode the electric fields. Every minimal triangular cell of the lattice constitutes a plaquette, which determines the magnetic interaction through the field B. **(b)** Dual representation of the triangular lattice in the previous panel. This yields a hexagonal lattice with spins on its sites, which are associated to the center of the initial plaquettes. **(c)** Representation of this hexagonal spin model on a Rydberg array. Every site is occupied by a "superatom", constituted by two atoms whose separation is $\eta < R_B$. Figure adapted from Ref. [35]

dimensional LGTs remains elusive. One of the main limiting factors that precludes the quantum simulation of LGTs in larger dimensions are the so-called *plaquette interactions*, which involve many-body relations, and are severely challenging to implement experimentally. In the case of electrodynamics, these terms are associated to magnetism.

The long term goal of the new experiment that we are building at ICFO is to provide a feasible platform on which these demanding plaquette terms can be implemented, allowing for the experimental realisation of LGTs in more than one spatial dimension. To start with, we aim to simulate the Rokhsar-Kivelson (RK) Hamiltonian, which is a 2D U(1) LGT originally formulated in the context of quantum spin ice and quantum dimers. Specifically, it depicts a spin ice in which a dynamic "plaquette flipping" term S competes with a "freezing" chemical potential ΛS^2,

$$H_{RK} = -\mathcal{J} \sum_p S - \Lambda S^2, \tag{7}$$

where $\mathcal{J}$ and Λ govern the energy scales of the first and second terms, respectively. The summation encompasses all the plaquettes of the system. This expression can be motivated through the Hamiltonian formulation of electromagnetism as a LGT [34, 35].

We will follow the novel theoretical proposal depicted in Ref. [34], in which a *dual formulation*, allowing for a great simplification of the plaquette interactions, is presented. The authors show that Rydberg atoms in configurable arrays naturally implement their approach.

Optical tweezers allow for trapping and moving very small objects by using a high numerical aperture lens that tightly focuses a laser beam, leading to a radiation force that holds the object in a fixed spot. Their technical development has enabled the arrangement of arrays of ultracold atoms with almost arbitrary geometries. The relatively large spacing—compared with the case of optical lattices—between adjacent sites in these arrays (of the order of several μm) prevents interactions between atoms through tunnel effect. Nonetheless, it is possible to generate interatomic interactions through Rydberg excitations. Rydberg states are characterised by the presence of at least one electron with a very high principal quantum number. Rydberg atoms have a large radius, long lifetimes, and they interact strongly through dipole-dipole and van der Waals interactions [5]. A key property is the Rydberg blockade mechanism: only single atomic Rydberg excitations within a given blockade radius R_B are allowed, since double excitations are strongly suppressed by large energy shifts from Rydberg van der Waals interactions. This is very suitable for

simulating spin models, and it is fundamental for our experiment proposal, as explained in the following.

We plan to study the RK Hamiltonian given in Eq. (7) in a triangular lattice. Its dual formulation translates into a hexagonal lattice whose sites are occupied by spins linked to the corresponding plaquettes. The promising approach that our theory collaborators proposed in Refs. [34, 35] for mapping this spin model to a Rydberg array involves substituting each lattice site by a pair of nearby sites, forming what is called a "superatom". Making the distance between the atoms in the same pair smaller than the blockade radius ensures that only one of them can be excited to the Rydberg state, thanks to the blockade mechanism. Thus, the spin orientation on each site can be encoded through the position of the excitation in the pair. For example, we can map the spin state $|\uparrow\rangle$ ($|\downarrow\rangle$) to the "superatoms" in which the Rydberg excitation sits on the right (left) atom conforming the pair. Figure 4 illustrates this scheme.

Using this configuration, we would be able to prepare the system in the ground state of the fully flippable phase of the RK model, which is mapped to a ferromagnetic spin configuration in the dual lattice—with all the spins pointing in the same direction—, by exciting all the atoms on the same side (left or right) of the "superatoms". Furthermore, other phases in this model can be accessed through the manipulation of the plaquette interactions. In the context of the Rydberg tweezer array, these are controlled by the Rabi coupling between the ground and Rydberg states. The effective Rabi frequency, which is linked to the term $\mathcal{J}$ in Eq. (7), depends on the detuning of the laser driving the Rydberg transition. Moreover, Rydberg interactions with other pairs mimic the second (Λ) term of the RK Hamiltonian. Therefore, the proposed experiment would allow for the exploration of the phases of the RK model by means of the adiabatic ramping of the Rabi coupling. Rydberg transitions with large Rabi frequencies are very beneficial for the proposed scheme. This is one of the main reasons for choosing strontium as our atomic species, as we explain in the next section.

3.2 Choosing strontium as the atomic species

The first ultracold neutral atoms experiments were based on alkaline elements, due to their simple electronic structure. Nonetheless, it was soon demonstrated that using other atomic species broadens the opportunities for quantum simulation. In particular, alkaline-earth atoms, which possess two valence electrons, have gained the attraction of the scientific community over the last decades [36–39]. The relative spin orientation of their two valence electrons allows for singlet and triplet states, with a total spin quantum number of $S = 0$ and $S = 1$, respectively. This leads to a rich energy level diagram, including broad transitions between states within the same singlet or triplet manifold, and narrow intercombination lines connecting both of them. These last transitions do not obey the selection rule preventing spin flips, $\Delta S = 0$, but they can be weakly allowed thanks to spin-orbit coupling.

We are particularly interested in alkaline-earth atoms because their two valence electrons allow for the simultaneous trapping of the atoms with optical tweezers and their excitation to Rydberg states. In the present work, we focus on strontium, an alkaline-earth atom with very suitable properties for the implementation of the theoretical scheme described in Sec. 3.1. Its atomic number is $Z = 38$, and it has four stable isotopes, whose relevant information for this work is collected in Table 1. In our experiment, we plan to use the most abundant isotope, ^{88}Sr. Its zero nuclear spin leads to the absence of hyperfine structure, easing its experimental manipulation (including the laser cooling stages, as discussed in Sec. 2).

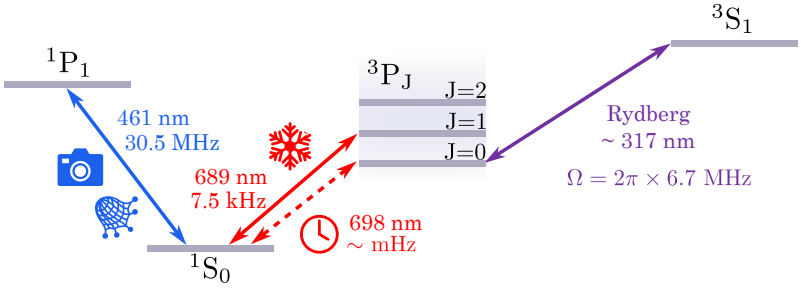

Figure 5: Strontium energy level diagram with the relevant states and transitions for the experimental scheme. Figure partly adapted from Ref. [39].

Isotope	Natural abundance	Statistics	I	$^1S_0 \leftrightarrow {}^1P_1$ isotopic shift (MHz)
^{88}Sr	82.58%	Bosonic	0	0
^{87}Sr	7.00%	Fermionic	9/2	-46.5
^{86}Sr	9.86%	Bosonic	0	-124.8
^{84}Sr	0.56%	Bosonic	0	-270.8

Table 1: Natural abundance, statistics, nuclear spin I and isotopic shifts in the $^1S_0 \leftrightarrow {}^1P_1$ transition for the natural isotopes of strontium.The isotopic shifts are referenced with respect to the most abundant isotope, ^{88}Sr. In this last column, the hyperfine structure of the fermionic isotope ^{87}Sr has been neglected, and a theoretical $I = 0$ state has been assumed. The amplitude of the hyperfine structure is larger than the isotopic shift, but its consideration is not needed in the scope of this work. Data taken from Ref. [40].

The optical transitions of strontium which are relevant for this experiment are depicted in Fig. 5 [37, 40]. The ground state $^1S_0$ ([Kr] $5s^2$) belongs to the singlet manifold. This work addresses the blue broad transition at 461 nm, which connects it with the first excited singlet state $^1P_1$ ([Kr] $5s\,5p$). This transition has a linewidth of $\Gamma_{\text{blue}} = 2\pi \times 30.5$ MHz, which yields a large range of atomic velocities that can be slowed down through laser cooling—as explained in Sec. 2—, but it also involves a relatively high Doppler temperature of $T_{\text{D,blue}} = 730\,\mu$K. In addition, the blue wavelength of this transition is very convenient for imaging purposes, since it allows for a high spacial resolution.

Moreover, strontium has a much narrower transition at 689 nm between the states $^1S_0$ and $^3P_1$ ([Kr] $5s\,5p$), connecting the singlet and triplet manifolds. The natural linewidth of this transition is 7.4 kHz, leading to a Doppler temperature of only $T_{\text{D,red}} = 179$ nK. Hence, further cooling can be achieved by exploiting this transition. As aforementioned, even though there is a spin change in this transition ($\Delta S \neq 0$), it is weakly allowed due to spin-orbit coupling.

Another noteworthy transition between the singlet and triplet manifolds is found at 698 nm, connecting the ground state $^1S_0$ with the $^3P_0$ ([Kr] $5s\,5p$) state. This transition is doubly forbidden by the selection rules: it does not only involve a spin flip, but it also connects two states with null angular momentum J. In the case of the fermionic isotope ^{87}Sr, whose nuclear spin is $I = 9/2$, the nuclear magnetic dipole moment couples the $^3P_0$ state to states with the same parity and $J = 1$, such as $^3P_1$ and $^1P_1$ [41]. This phenomenon is known as *hyperfine interaction mixing*, and it enables a single photon E1 transition to the ground state with a lifetime of approximately 100 s, and a linewidth of $\Gamma = 2\pi \times 1.6$ mHz. Due to this ultranarrow linewidth, it is utilised in the most precise atomic clocks to date, and it is typically referred to as *clock transition*.

Nonetheless, for the bosonic isotopes of strontium—as the one which we will be using—the nuclear angular momentum is zero, and the $^3P_0$ state decays via a two-photon process, encompassing an electric and a magnetic dipole transitions (E1M1). Therefore, the $^3P_0$

state has an estimated decay time of the order of 10^3 years, hence behaving as an effective ground state. This property will be exploited in our experiment, since it allows for an effective "single" photon Rydberg excitation, connecting the metastable clock state $^3P_0$ and the Rydberg state $^3S_1$ ([Kr] $5s\,61s$), with a wavelength of 317 nm. This direct Rydberg excitation has a large Rabi frequency, which is very favourable for our strategy to access different phases of the RK model, presented in Sec. 3.1.

3.3 Plan for the experimental sequence

The experimental manipulation of ultracold atoms requires reaching quantum degeneracy conditions, which imply extremely low temperatures and high vacuum pressure levels. To this end, a system composed of a high-vacuum and a ultra high-vacuum region (with pressure values of the order of 10^{-10} and 10^{-12} mbar respectively), inspired by the apparatus constructed in Ref. [39], will be utilised. The initial steps in the experimental sequence that will be followed aim to cool down the strontium atoms to the temperatures allowed by laser cooling.

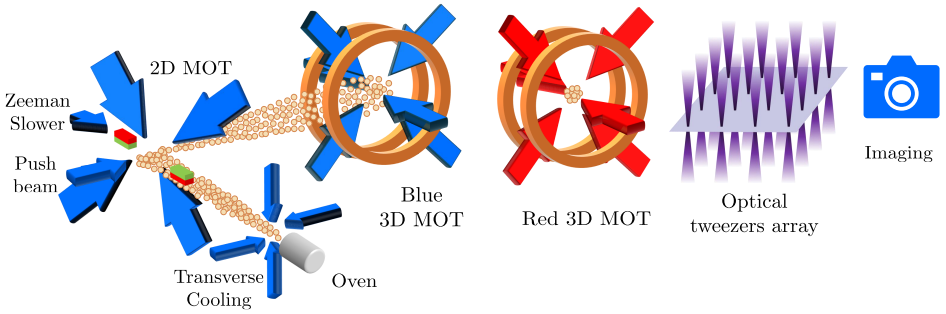

Figure 6: Plan for the experimental sequence. Figure adapted from Ref. [39].

Strontium is solid at room temperature, and it has a low vapour pressure compared to alkali atoms. Thus, it is necessary to heat it up to higher temperatures in order to obtain an initial atomic cloud. In our experiment, an oven at about 450°C will be employed to this end. The angular divergence of the atomic beam will be reduced via the so-called *transverse cooling* technique. This consists of using Doppler cooling (explained in detail in Sec. 2) in two perpendicular directions with respect to the atomic beam. Then, the longitudinal velocity of the atoms will be reduced by a Zeeman slower, and they will be subsequently trapped in a transverse 2D MOT [38, 42]. Subsequently, a resonant push beam will transfer the atoms from the high-vacuum section into a science chamber in the ultra high-vacuum region, where a 3D MOT will be used to capture the atomic cloud. All of these initial cooling steps will operate on the blue $^1S_0 \leftrightarrow {}^1P_1$ transition at 461 nm, since, as discussed in Sec. 2, its large linewidth allows for greater *capture velocities*. This term refers to the initial velocity range of the captured atoms. Naturally, faster capture velocities lead to a larger atomic flux in in the 3D MOT chamber. However, the width of the transition also implies that the blue laser will only allow us to reach temperatures of a few mK. Afterwards, the strontium atoms will be further cooled into the μK regime using a red 3D MOT on the narrow $^1S_0 \leftrightarrow {}^3P_1$ transition at 689 nm. The captured atoms will be loaded in a tailored tweezer-array, which will be manipulated using Rydberg excitations to study the RK model, as discussed in Sec. 3.1. Finally, blue light at 461 nm, combined with simultaneous cooling at 689 nm [43], will be used for imaging the realised simulations. The described steps for the experimental sequence are displayed in Fig. 6.

4 Laser system at 461 nm

In this section, we present the main results of this project, which has been devoted to the construction of the blue laser system on the 461 nm transition.

4.1 Prerequesites and estimation of parameters for the laser system

The laser system needs to provide light for all the tasks requiring blue light described in Sec. 3.3, i.e. the initial cooling stages and imaging. This light will be sent to the experiment through optical fibers. In the following, we address three key features that the blue laser system needs to fulfill.

- **Active frequency stabilisation.** Avoiding frequency drifts is essential for exciting the atomic transition, and for ensuring precise and repeatable measurements. To this end, we use an active stabilisation scheme based on spectroscopy, which is described in detail in Sec. 4.2.

- **Frequency detunings.** The cooling strategy requires laser beams which are slightly detuned from the atomic resonance frequency. Acousto-optical modulators provide the necessary control of the frequency shifts for every task. Section 4.3 is devoted to them.

- **Optical power.** The width of the $^1S_0 \leftrightarrow {}^1P_1$ transition also yields a high saturation intensity $I_{\text{sat}} = 40.7\,\text{mW/cm}^3$. In order to attain the required optical power for each cooling stage, our system needs to incorporate high power laser sources (providing hundreds of mW). These are generally associated with high levels of noise and frequency fluctuations, typically even emitting light at multiple frequencies. However, it is possible to reach high optical power while guaranteeing a low-noise single-mode performance by means of *injection locking*. In this technique, some light from a low power single-mode *master* laser is sent into a high power laser—referred to as *slave*—, whose frequency range is relatively close to that of the former. Thereby, their emission is coupled, and the slave is forced to emit exactly on the master's frequency [44]. Thus, single-mode operation and frequency stabilisation of the high-power slave laser are achieved. Specifically, four slave lasers will be used in our system, and the stability of their injection lock will be monitored in a Fabry-Pérot cavity. The characterisation of a slave laser and the monitoring setup are presented in Sec. 4.4.

In order to estimate the optimal frequency detunings and optical power for each specific cooling stage, we perform numerical Monte Carlo simulations[1]. The results for the Zeeman slower are shown as an example on Fig. 7. Therein, we sweep a range of possible values for the detuning (left panels) and the optical power (right panels), and we calculate the associated capture velocity v_c (top panels) and the trapped fraction of atoms n_{tr}, which is defined as the ratio of captured atoms over the total number of atoms considered in the simulation (bottom panels). This method gives an estimation of the optimal parameters—which will be further optimised empirically once the experiment is ready—, and it also provides information on the influence of deviations around each of them. For the Zeeman slower example in Fig 7, we appreciate that the frequency plays a fundamental role, with an approximated optimal detuning $\delta_{\text{ZS}} \simeq -16\Gamma$; whereas no local maxima are found with respect to the power, and higher values always seem to lead to better results (therefore, we

[1] In this project we looked for the optimisation of the detuning and power parameters using a code developed by Carlos Gas Ferrer [45] and Ana Pérez Barrera, fellow members of the QGE group.

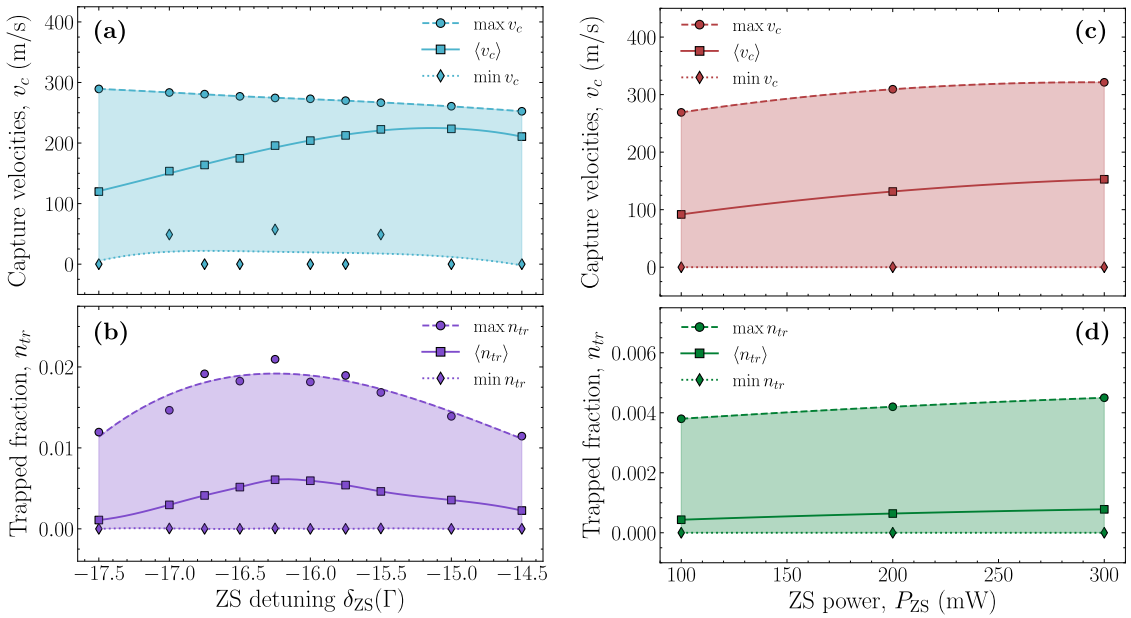

Figure 7: Monte Carlo simulation results for the estimation of the Zeeman slower (ZS) parameters. The capture velocities v_c (top panels) and trapped fractions of atoms n_{tr} (bottom panels) for different values of the detuning (left) and the optical power (right) are displayed. The range of v_c and n_{tr} values yielded by the simulation are shadowed. In each panel, we also show the maximum, average, and minimum values obtained (circles, squares, and rhombus, respectively), as well as the corresponding interpolation curves for these data points (dashed, solid, and dotted lines, respectively).

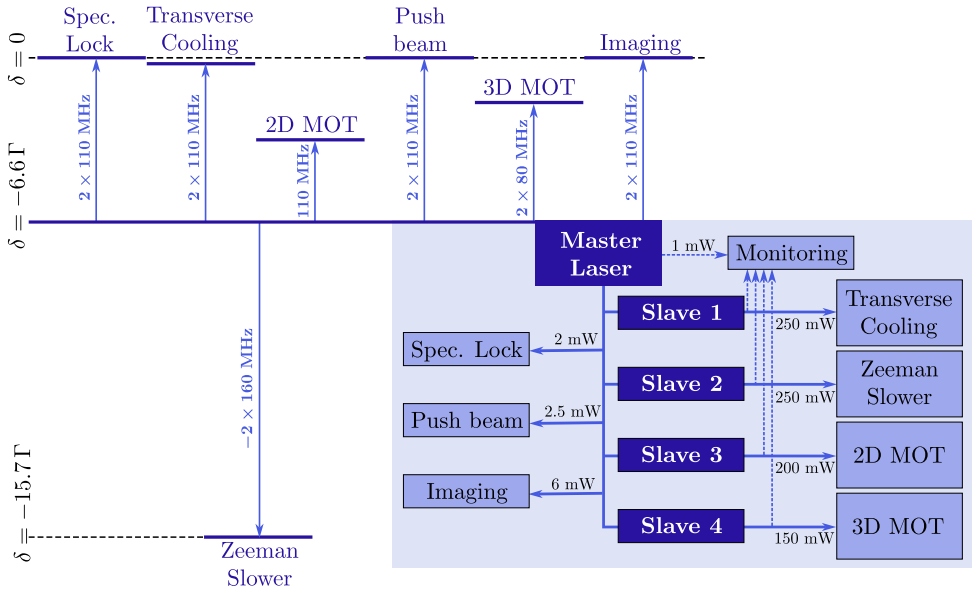

Figure 8: Blue laser system overview. The master laser will be red detuned with respect to the $^1S_0 \leftrightarrow {}^1P_1$ transition with $\delta = -6.6\Gamma$. All the cooling beams (transverse cooling, Zeeman slower, 2D and 3D MOTs) are also red-detuned, whereas the spectroscopy lock, the push and imaging beams are resonant. The displayed values in the power distribution scheme correspond to the final power planned to be sent to each application. Therefore, the total power of the laser system needs to be higher than their sum, since we need to take into account the power losses due to multiple factors, such as the fiber coupling efficiencies.

need to consider the experimental constraints). Thus, our simulations allow us to assign nominal frequency shifts and optical power values for each purpose of the blue laser system, which are displayed in Fig. 8.

4.2 Spectroscopic stabilisation of the master laser

We utilise an external cavity diode laser (ECDL) in the Littrow configuration as the master laser[2] providing light at 461 nm. Its description is provided in Appendix B. Generally, diode lasers are extremely sensitive to environmental factors (e.g. diode current fluctuations, temperature changes or mechanical vibrations), and a laser frequency stabilisation is therefore required. To this end, we establish an active spectroscopic feedback scheme. It is possible to lock the laser frequency to an artificial reference, such as an optical cavity, but we choose to do it directly on the atomic transition through absorption spectroscopy to promote long-term stability.

4.2.1 Experimental apparatus

The spectroscopy setup is based on a vapour cell designed by a previous master student in our group [46]. It is shown in the first panel of Fig. 9, and it consists of a pipe made of stainless steel with a reservoir at its center, where the strontium is deposited. This chamber is closed with a DN25 flange, easing the refilling process, and it is surrounded by a collar heater[3] that enables the evaporation of strontium. Anti-reflection coated glass windows are placed at both ends of the heat pipe, through which the light beams can go and interact with the atomic cloud. These viewports are tilted at 8° with respect to each other to prevent internal reflections of the laser beams from producing interference.

Strontium is a highly reactive element, and impeding that it coats the viewports is essential for elongating the lifetime of the apparatus. On the one hand, the solid angle under which the strontium atoms can reach the windows in direct flight is reduced by choosing a small—but yet wide enough for a sufficient light-matter interaction—diameter for the tube (8 mm), and a long distance between the viewports and the reservoir (30 cm). On the other hand, a buffer gas (typically a noble gas, as argon in our case) is introduced to reduce the probability of strontium atoms hitting the windows, as they are dispersed through collisions with this gas. The typical total pressure values in a cell for a spectroscopy lock are about $10^{-3} - 10^{-4}$ mbar, given by the buffer gas pressure [47].

Although the heat pipe was thought to be ready for use when this project was planned, we found out that there was a compact agglomerate of strontium, strongly attached to the inner walls of the heat pipe, blocking the beam path. We think that this had been caused by a large vertical temperature gradient in the central chamber of the heat pipe. In the past, the collar heater surrounding the low part of the reservoir was used to reach very high temperatures of about 600 °C. The top region of the chamber did not receive direct heating, and the strontium supply, which may had been fully sublimated at this temperature range, was displaced to the coldest available area: the inner facet of the DN25 flange and the uppermost sections of the inner walls of the chamber, as you can see in photos (b) and (i) in Fig. 9. Diverse ideas for solving this problem were considered, and we finally decided to open the heat pipe and let the strontium oxidise. This solution was inspired by the fact that the strontium oxide is a granular substance which could be easily removed from the apparatus by periodically scraping with a tool. The evolution of the oxidation process

[2] Moglabs, ILA-A52103016

[3] Watlow St. Louis, MB2A1JN1-B12

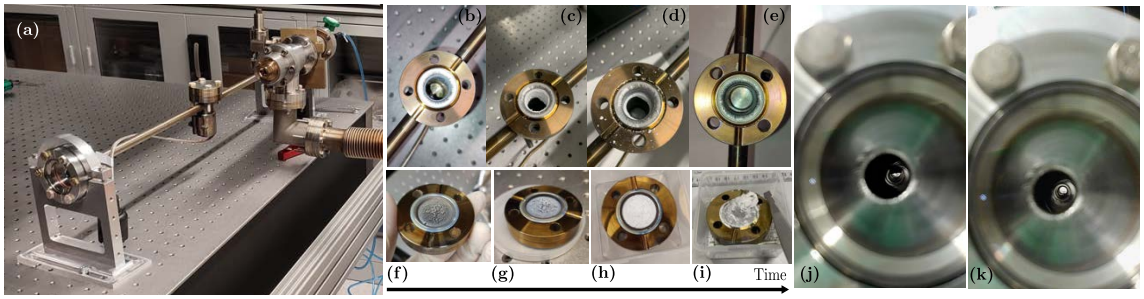

Figure 9: **(a)** Heat pipe for the spectroscopy lock. The photographs **(b)-(e)** show the temporal evolution of the strontium block seen from above the main chamber. Images **(f)-(i)** show the oxidation of the strontium attached to the interior of the DN25 flange removed from the heat pipe, which inspired our approach to solve the problem. The photographs **(j)** and **(k)** show the view from one of the ends of the pipe towards the other, before and after removing the block.

is also shown in Fig 9. The followed approach entailed the need for restoring the high vacuum in the heat pipe, and refilling the reservoir with new strontium. This procedure is described in Appendix C, and in my master internship report [48].

4.2.2 Doppler-free spectroscopy

In absorption spectroscopy, spectral lines can be widened by both homogeneous and inhomogeneous mechanisms. A paradigmatic example in the first category is the natural broadening caused by the finite lifetime of the excited state, which affects equally all atoms of the same species. On the contrary, the Doppler effect induces inhomogeneous broadening, since it depends on the velocity of each individual atom. As mentioned in Sec. 2, the Doppler effect induces a frequency shift given by $\omega_D = -\vec{k} \cdot \vec{v}$, where $\vec{k}$ is the radiation wavevector and $\vec{v}$ is the atom velocity. Let us recall that throughout this text ω_0 and ω denote the atomic transition and laser frequencies, respectively, and $\delta \equiv \omega - \omega_0$ is the light detuning. Due to the Doppler effect, light is not only absorbed when the resonance condition $\omega = \omega_0$ is strictly verified. Instead, off-resonant light is also absorbed by atoms whose velocity yields a Doppler shift that compensates for the detuning,

$$\delta \equiv \omega - \omega_0 = \vec{k} \cdot \vec{v}. \tag{8}$$

Even for broad transitions, as the one which is considered throughout this work, the Doppler effect embodies the major contribution to the broadening of spectral lines, frustrating high-precision laser locking. This limitation can be overcome through several techniques. In this thesis, we explore saturated absorption spectroscopy (SAS), particularly the method of modulation transfer spectroscopy (MTS).

Saturated absorption spectroscopy

When a light beam passes through an atomic cloud, the intensity variation with respect to the crossed distance obeys a Beer-Lambert's law type of equation [33],

$$\frac{dI}{dl} = -\kappa(\omega) I, \tag{9}$$

where I is the light intensity, l is the spatial coordinate in the direction of the beam, and $\kappa(\omega)$ is the absorption coefficient at frequency ω of the incident photons. This coefficient is given by

$$\kappa(\omega) = \int \left[N_g(v) - N_e(v)\right] \sigma(\omega - kv)\, dv, \tag{10}$$

where $N_g(v)$ and $N_e(v)$ denote the number density of atoms in the ground and excited states, respectively, whose velocity component along the beam direction is $v \equiv \vec{v} \cdot \vec{k}/k$. Here, $\vec{v}$ is the total velocity, $\vec{k}$ is the light wavevector and k is its amplitude. The absorption cross section is designated by σ, and it is a function of the light frequency in the atom's frame of reference: $\omega' \equiv \omega + \omega_D = \omega - \vec{k} \cdot \vec{v} = \omega - kv$. It has a Lorentzian profile,

$$\sigma(\omega') \equiv \frac{g_e}{g_g} \frac{\pi^2 c^2}{\omega_0^2} A_{21} L(\omega' - \omega_0; \Gamma), \tag{11}$$

where g_g[4] (g_e) is the degeneracy factor of the ground (excited) level, c is the light speed, A_{21} is the Einstein coefficient for spontaneous emission and $L(\delta; \Gamma)$ is the Lorentzian function given in Eq. (1). Generally, the natural linewidth is much narrower than the Doppler broadening, and therefore the Lorentzian in Eq. (11) can be approximated by a delta function of $\omega' - \omega_0$. Hence, the absorption coefficient is approximately proportional to the population difference between the two energy levels for atoms in which the effective resonance condition given in Eq. (8) is verified, i.e. with $v = \delta/k$,

$$\kappa(\omega) \propto N_g(\delta/k) - N_e(\delta/k). \tag{12}$$

The SAS technique is based on this phenomenon. It requires the superimposition of two counter-propagating laser beams of the same frequency ω through the medium on which spectroscopy is performed, which are typically referred to as *pump* and *probe* beams. The former is usually more intense, and it excites many of the atoms for which the associated resonance condition is verified (in their frame of reference) to the upper energy level. Hence, the quantity $N_g(v) - N_e(v)$ is significantly reduced for atoms such that $\vec{v} \cdot \vec{k}_{\text{pump}} = \delta$. This phenomenon is known as *hole burning*. If we now consider the absorption of the counter-propagating probe beam, according to Eq. (12), it will be approximately proportional to $N_g(v) - N_e(v)$, but with $\vec{v} \cdot \vec{k}_{\text{probe}} = \delta$. Since the pump and probe beams have opposite wavevectors, the only velocity class for which they interact with the same atoms is that in which $v \simeq 0$. The depletion of the ground state population by the pump beam reduces the absorption of the probe beam, giving rise to a narrow peak in the intensity of the probe beam transmitted through the gas. The corresponding valley in the absorption spectra is usually referred to as *Lamb-dip*. This Doppler-free signal precisely appears at the actual resonance frequency, when $\delta = \omega - \omega_0 = 0$. The SAS principle is illustrated on the left panel in Fig. 10.

The schematics of the experimental setup is shown in Fig. 11, in which we shall not consider the blue shadowed region for the moment. The seed laser is connected to a function generator that produces a voltage ramp which induces a linear frequency scanning by driving the main piezo electric actuator that controls the external cavity length of the ECDL (see Appendix B for details on the ECDL in Littrow configuration). In the spectroscopy setup, the main beam is divided into the pump and probe beams with a polarising beam splitter (PBS). A preceding half-wave plate is used to control the power ratio between both beams. Two Keplerian telescopes, consisting of two convex lenses (with focal lengths of 50 mm for L5, L7 and 300 mm for L6, L8) are used to amplify the pump and probe $1/e^2$ beam diameters from 0.6 mm to 3.6 mm, approximately. Both beams meet through the heat pipe. We compared the signal-to-noise ratio for linearly and circularly polarised pump and probe beams—polarisation has a decisive role in MTS [49]—, and the optimal configuration was found to correspond to circular and orthogonal

[4] For bosonic strontium, $g_g = 1$, since $S = 0$ and $I = 0$.

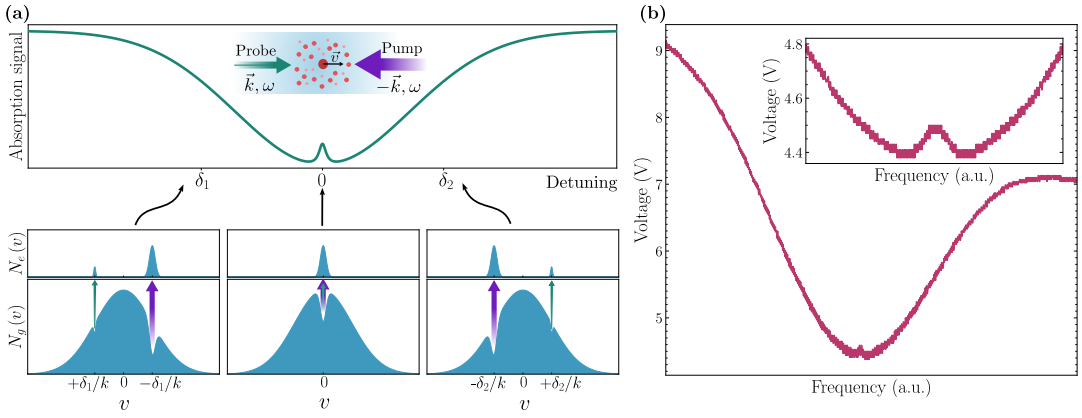

Figure 10: **(a)** Saturated absorption spectroscopy principle. **(b)** Experimental SAS signal. The inset on the focuses on the Doppler-free peak, reducing the span of the frequency scan. These data were collected at a reservoir temperature of $T = 360°\mathrm{C}$.

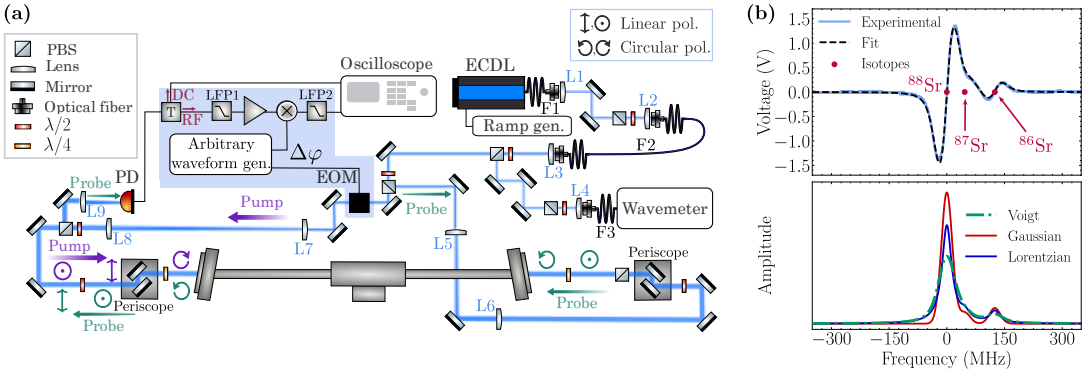

Figure 11: **(a)** Schematics of the spectroscopy setup[5]. The elements in the highlighted blue box are only needed for MTS. **(b)** Experimental MTS results at temperature $T = 365°\mathrm{C}$. On the top panel, the MTS signal (light blue solid line) and the associated fit (dashed black line) are plotted. The three red circles give the transition frequencies (with respect to that of ^{88}Sr), for the isotopes ^{88}Sr, ^{87}Sr, and ^{86}Sr, from left to right. In the bottom right panel, the sum of the Lorentzian (blue solid line), Gaussian (red solid line) and Voigt (dashed green line) curves for the three isotopes are shown. The Lorentzian profile is associated to the natural lineshape of the transition, whereas the Gaussian distribution is obtained through the fit. As mentioned in the main text, the Voigt profile is their convolution.

polarisations (σ^+-σ^-/σ^--σ^+). After going through the heat pipe, the probe beam is sent to a photodetector (PD), and the spectroscopy signal is monitored in an oscilloscope.

The direct transmittance signal of the probe beam, shown on the right panel in Fig. 10, is far from ideal for laser locking purposes: the Doppler-broadened spectrum remains as a background, the relative amplitude of the Doppler-free peak is quite small, we have no references for calibrating the frequency axis, and it is symmetric with respect to the resonance point, hindering the laser locking. More elaborated SAS methods have been developed in order to overcome these limitations. Specifically, we focus on modulation transfer spectroscopy, which is explained in the following.

[5]List of components: seed laser *Moglabs, ILA-A52103016*; electro-optic modulator *Qubig, PM7-VIS-15*; ramp generator *GW Instek, SFG-1003*; wavemeter *HighFinesse GmbH, WS7-60*, arbitrary waveform generator *RIGOL, DG2102*; oscilloscope *Rigol, DS1054Z*; photodetector *Thorlabs, PDA10A2*; fiber F1 *Schäfter+Kirchhoff, PMC-E-460Si-4.0-NA009-3-APC-DC-200-P*; fibers F2, F3 *Thorlabs, P3-405BPM-FC-1*; collimators L1, L2 *Schäfter+Kirchhoff, 60FC-SF-4-A4.5S-01*; lenses L5, L6, L7, L8, L9 *Thorlabs, LA1131-A, LA1484-A-ML, LA1131-A-ML, LA1484-A, LA1509-A*; fiber in-coupler lenses L2, L4 *Thorlabs, C330TMD-A, C610TME-A*; polarising beam splitters *Foctek, PBS5204 (H-ZF2)*; mirrors *Thorlabs, BB1-E02*, $\lambda/2$-plates *Foctek, WPL212H*, $\lambda/4$-plates *Foctek,*

Modulation transfer spectroscopy

In this technique, the phase of the pump beam is modulated, typically with an electro-optic modulator (EOM) [50–52], as we do here. This modulation is transmitted to the probe beam by means of *four wave mixing*, an effect arising from the propagation of different frequency components in a nonlinear medium. The underlying physical phenomenon is briefly described in Appendix D. The transferred modulation can be measured through a phase-sensitive signal processing technique known as *heterodyne detection*, which is also described in Appendix D . This allows for the obtention of an error signal which is proportional to the derivative of the original spectral feature, as explained in the aforementioned appendix.

One key property of the above-described modulation transfer is that it only occurs when the sub-Doppler resonance condition is fulfilled. Thereby, the MTS signal baseline is almost independent of the residual linear absorption effect, leading to a robustly flat and null background, contrary to the direct transmittance signal of the probe beam in SAS (see Fig. 10b). In addition, the signal has a zero-crossing precisely at the resonance frequency (where there is a local maximum in the direct absorption). This is very beneficial for the electronic lock, which will be discussed later. In order to perform MTS, we simply need to incorporate an EOM[6] and various electronic components to the previously described experimental setup (see the blue highlighted region in Fig. 11a).

The obtained MTS signal allows for the detection of three of the four natural isotopes of strontium, with the only exception of ^{84}Sr, which is the least abundant. Indeed, the frequency scale presented in Fig. 11 was calibrated by taking into account that the separation between the zero-crossings of the MTS signal corresponds to the isotopic shift between ^{88}Sr and ^{86}Sr. Let us recall that the relevant information about the natural isotopes of strontium for this work is collected in Table 1 in Sec. 3.2.

The measured MTS signal can be fitted as we explain in the following. Ideally, the spectral line shape in absorption spectroscopy is described by a Lorentzian profile, whose mathematical formulation was given in Eq. (1). Nonetheless, we also need to take into account the collisional broadening, enhanced by the buffer gas included in the heat pipe, which can be assumed to have a Gaussian distribution. Thus, we obtain a Voigt profile, defined as the convolution of the Lorentzian and Gaussian functions,

$$V(\delta;\Gamma,\sigma) \equiv \int_{-\infty}^{+\infty} d\delta' G(\delta';\sigma) L(\delta-\delta';\Gamma), \tag{13}$$

where $G(\delta';\sigma) \equiv \exp(-\frac{\delta'^2}{2\sigma^2})/(\sqrt{2\pi}\sigma)$, and σ denotes the Gaussian standard deviation.

Furthermore, the signal that we measure is proportional to the derivative of the Voigt profile, due to the modulation-demodulation procedure, as we explain in Appendix D. Thus, we fit our data with the following expression,

$$f(\delta;C,\sigma) = C\left[\sum_{j=86}^{88} \frac{C_j}{C_{88}} \frac{dV}{d\delta}(\delta-\delta_j;\Gamma,\sigma)\right], \tag{14}$$

where C_j and δ_j denote, respectively, the natural abundance and the isotopic shift of ^{j}Sr, with $j \in \{86, 87, 88\}$. C is simply an overall amplitude factor. Herein, we have assumed that the isotopic distribution in our sample coincides with the natural abundances.

WPL212Q; bias-T *Mini-Circuits, ZFBT-4R2GW+*; mixer *Mini-Circuits, ZFM-1W-S+*; amplifier *Mini-Circuits, ZFL-500LN+*; low pass filters LPF1 *Mini-Circuits, 15542, BLP-25+ LPF*, LPF2 *home-made*.

[6] Qubig, PM7-VIS-15. We use a modulation frequency of 15 MHz, which is approximately half of the natural linewidth of the transition of interest, being close to reported optimal ratios [53].

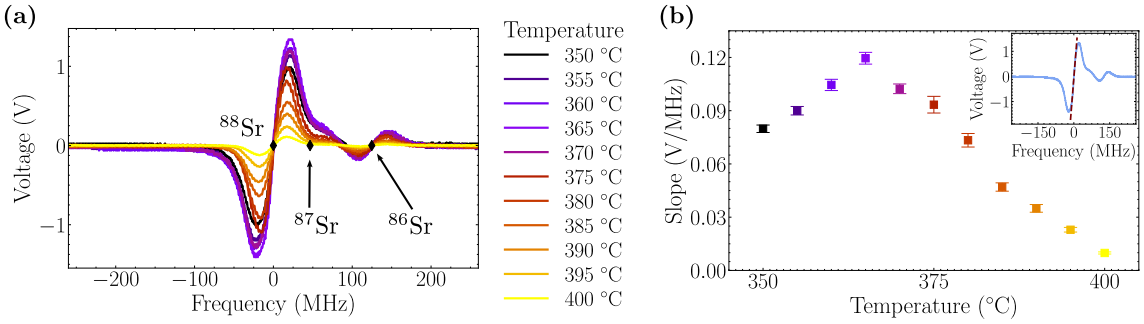

Figure 12: Temperature dependence of the MTS signal. **(a)** MTS signal for temperatures between 350°C and 400°C. The black rhombuses represent the three detected isotopes. **(b)** Slope of the signal at the zero crossing corresponding to ^{88}Sr vs. the temperature of the heat pipe.

The result of this fit is displayed on the top right panel of Fig. 11. The resulting value of the Gaussian standard deviation was found to be $\sigma = (14.22 \pm 0.06)$ MHz, and $C = (-3935 \pm 16)$ V, where the errors correspond to a 68% confidence interval. The coefficient of determination of the fit is $R^2 = 0.994$. The sum of the Lorentzian and Gaussian profiles for each detected isotope, as well as the sum of their respective convolutions, giving the Voigt distributions, are displayed in the right bottom panel of the figure.

Furthermore, we studied the MTS signal dependence on the temperature of the strontium atomic cloud. The measured signal for temperatures between 350°C and 400°C, after optimising the power of the pump and probe beams in each case, are displayed on the left panel of Fig. 12. The corresponding slope values at the zero-crossing of ^{88}Sr for these MTS signals as a function of the temperature are plotted on the right panel. We observe that the optimal signal is attained at 365°C.

4.2.3 Laser locking

The MTS method described in the previous section provides a suitable signal for laser frequency stabilisation [49–53]. For this purpose, we use a proportional integral (PI) controller that drives the main piezo electric actuator in the ECDL so that the laser frequency always matches the zero crossing in the MTS signal. Thus, the PI circuit serves as a feedback loop controller that holds the system at the desired lock point, by conveniently adjusting the electric signal sent to the piezo actuator as a function of the error between the set point and the actual value of the variable. In our case, the error is the voltage difference between the MTS zero crossing ($V_0 \equiv 0$) and the measured voltage $V_\delta(t)$, which depends on the detuning: $\varepsilon(t) \equiv V_0 - V_\delta(t)$. Naturally, this requires reducing the amplitude of the frequency scan so that there is a single zero-crossing (specifically, the one corresponding to ^{88}Sr). The output of the PI control circuit is given by [54]

$$U(t) \equiv K_p\, \varepsilon(t) + K_i \int_0^t \varepsilon(\tau)\, d\tau, \tag{15}$$

where K_p and K_i are the proportional and integral gains, respectively, which are experimentally optimised. The proportional term depends on the present error, while the integral term collects information about the accumulated past error. It is also possible to use proportional integral differential (PID) circuits, in which a differential term $K_d\, d\varepsilon/dt$, accounting for the prediction of future error, is additionally included. Similar PID loops are used to regulate the temperature stabilisation of laser diodes, as we will explain in Sec. 4.4.

The error signal over 60 ms for the locked master laser is shown in Fig. 13. The highlighted area corresponds to the standard deviation within this time interval, obtained

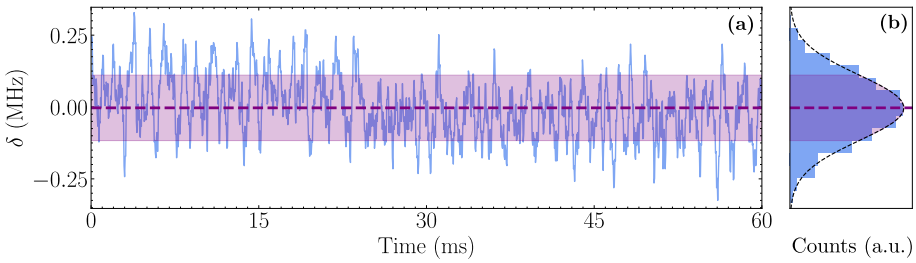

Figure 13: Master laser lock characterisation. Panel **(a)** shows the error signal of the locked master laser vs. time. The voltage variations as a function of time recorded in the oscilloscope are translated to frequency values by taking into account the V/MHz slope of the MTS signal around the ^{88}Sr zero-crossing (note that the laser frequency is held in the linear region around this lock point). The associated error histogram is displayed in panel **(b)**, where the dashed black line shows a Gaussian fit with a determination coefficient of $R^2 = 0.991$. The horizontal purple dashed line corresponds to the detuning mean value, and the highlighted area represents the standard deviation, obtained from the Gaussian fit.

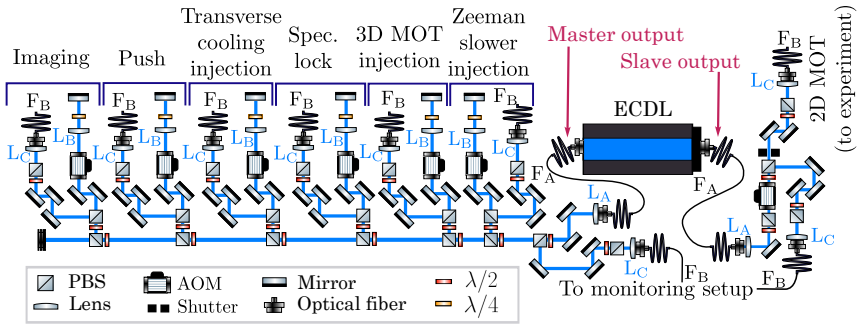

Figure 14: **(a)** Schematics of the laser system setup[7]. The master path has multiple PBSs that send light to the different AOMs in double-pass configuration (whose purpose is indicated above). The frequency-shifted light is sent to the different tasks through optical fibers. In addition, some light is sent to a monitoring setup with a Fabry-Pérot cavity. The built-in injected amplifier sends its light to a single-pass AOM, after which the beam splits in two paths: one that goes directly to the experiment table, including a previous shutter, and one going to the monitoring setup to check the slave injection.

by doing a Gaussian fit for the associated histogram, which is also displayed on the right panel of the figure. The obtained standard deviation is 114.1 ± 2.2 kHz. This value is much smaller than the natural linewidth of the $^1S_0 \leftrightarrow {}^1P_1$ transition, 30.5 MHz, so we can confirm that a successful laser lock has been achieved.

4.3 Frequency control: acousto-optical modulators

The laser system needs to provide independent frequency control for the different tasks for which it supplies light. To this end, we use acousto-optical modulators (AOMs), whose working principle and diffraction efficiency is described in Appendix E. Regarding their disposition, the approach that we have followed is to prioritise the use of double-pass AOMs in order to allow for modulation frequency scans. Naturally, we use them for the applications which do not need a lot of power (i.e. spectroscopy, push beam, imaging, and monitoring, as shown in Fig. 8); but we can also use this configuration for those demanding

[7]List of components: seed laser *Moglabs, ILA-A52103016*; fibers F_A *Schäfter+Kirchhoff, PMC-E-460Si-4.0-NA009-3-APC-DC-200-P*; fibers F_A *Thorlabs, P3-405BPM-FC-1*; collimators L_A *Schäfter+Kirchhoff, 60FC-SF-4-A4.5S-01*; lenses L_B *Thorlabs, LA1509-A*; fiber in-coupler lenses L_C *Thorlabs, C230TMD-A*; polarising beam splitters *Foctek, PBS5204 (H-ZF2)*; mirrors *Thorlabs, BB1-E02*; $\lambda/2$-plates *Foctek, WPL212H*, $\lambda/4$-plates *Foctek, WPL212Q*; shutter *home-made*; AOMs *IntraAction ATM-A1 series*—the central frequency for each case is depicted in Fig. 8.

high power (in the order of 100 mW) and hence a slave laser, by placing the AOM before the slave injection. Thus, the final power is not limited by the AOM diffraction efficiency, which only affects the intensity of the injected light. Of course, since the outgoing light is not directly sent to the experiment in this scheme, the AOMs do not serve as a switch in this case.

Nevertheless, one of our slave lasers is integrated in the commercial Moglabs system[2], so the associated AOM needs to be placed after injection. Consequently, we use a single-pass AOM in this case. Since the available power is more crucial for the Zeeman slower, we prefer to dedicate a home-made slave yielding all its power at the needed frequency, so we discarded using this slave for the Zeeman slower. In addition, a mechanical shutter is a sufficiently quick switch for this stage. Thus, among the cooling stages which require relatively high power without the need for sweeping the laser frequency, we choose to use the single-pass AOM for the 2D MOT.

The schematics of the main path of the laser system and the AOMs layout is displayed in Fig. 14.

4.4 Power amplification

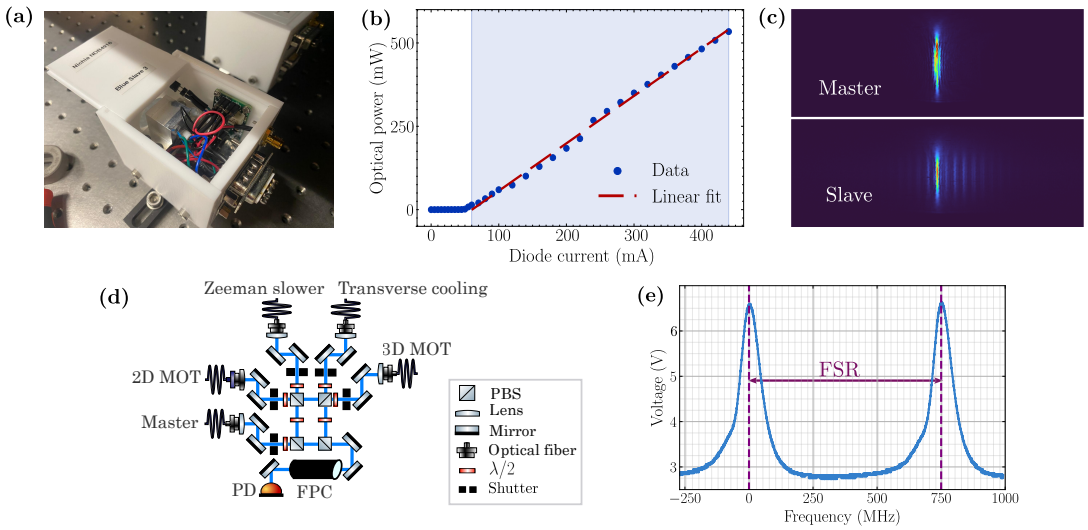

Figure 15: **(a)** Photograph of the assembled home-made slave laser. Inside the casing, a mechanical block is used to hold the diode and stabilise its temperature, altogether with the thermistor and TEC for implementing an active feedback. A homemade printed circuit board protects the laser diode from voltage spikes and electrical noise, two D-sub 9 adapters connect the system with the current and temperature controllers, and a collimation lens shapes the laser diode output[8]. **(b)** Plot of the optical power vs. the diode current for this slave, at $T = 23.4°\text{C}$. The dashed red line shows the linear fit within the highlighted range, with a determination coefficient of $R^2 = 0.997$. The zero-crossing of this line gives the threshold current $I_{\text{th}} = (60 \pm 4)$ mA, below which the diode emits incoherent light. **(c)** Master and slave lasers spectra on a home-made grating wavemeter[10], sending 1 mW of light in each case to the CCD camera with a ND=3.0 absorptive filter. **(d)** Schematics of the monitoring setup, based on a FPC[9]. **(e)** Spectrum of the cavity for the master laser light. We can calibrate the frequency in the horizontal axis by taking into account that the frequency difference between two consecutive peaks—outlined in purple color in the plot—is the free spectral range (FSR) of the confocal cavity, which is given by $\text{FSR} = c/(4L)$, where L is the length of the cavity and c is the light speed. Herein, L= 10 cm and FSR = 750 MHz.

[8]List of components: laser diode *Nichia NDB4916*; thermistor *Farnell 679446*; TEC *Multicomp PRO MCPE1-07106NC*; collimating lens *Newport KGA-671-A-MT*; current and temperature controllers *Toptica*.

[9]List of components: FPC *home-made*; optical fibers *Thorlabs, P3-405BPM-FC-1*; collimators *Schäfter+Kirchhoff,*

As we explained in Sec. 4.1, we need four slave lasers to reach the required power for the experimental purposes of the laser system. One of them is integrated in the commercial Moglabs laser device[2], and the other three slaves are home-made, based on commercial laser diodes and assembled following the design elaborated by a previous master student in the group [46]. Two of those were already assembled, and the third one, which can be seen on panel (a) in Fig. 15, was mounted during this master thesis project.

The diode emission depends on its current and temperature, both of which are externally controlled. The latter is sensed with a thermistor, and adjusted to the set value with a PI circuit operating on a Peltier thermoelectric cooler (TEC). The characterisation of the emitted optical power as a function of the diode current is shown on panel (b) in Fig. 15, where we obtained a threshold current of $I_{\mathrm{th}} = (60 \pm 4)$ mA. Therein, we also confirm that the laser diode can emit up to 500 mW, which demonstrates its suitability for our experiment. As previously outlined, high power laser diodes do not generally work in single-mode operation. This can be checked on panel (c) in Fig 15, where the master and slave lasers spectra on a previously built home-made grating wavemeter[10] are shown. Each vertical line on the image corresponds to a different frequency. Hence, we observe that the master laser operates indeed in single mode, but the unlocked slave laser does emit light on more than one frequency. This is precisely one of the key factors that motivate the need for injection locking from the master laser. The frequency stability of the slave lasers will be monitored with a Fabry-Pérot cavity (FPC), in addition to the previously mentioned grating wavemeter. The associated FPC monitoring setup was also built as part of this project, and its schematics is shown on panel (d) in Fig. 15. On panel (e), the spectrum of the master laser is shown.

5 Conclusion and outlook

In this thesis, we developed a laser system for a new cold atoms experiment. We performed the frequency stabilisation of the master laser via Doppler-free spectroscopy. First, we prepared the spectroscopy setup by baking out the heat pipe. Then, we explored SAS, and particularly MTS, which allowed us to optimise the signal and lock the laser successfully. In addition, we addressed the need for specific frequency shifts in each step of the cooling sequence, preparing a setup with the required acousto-optical modulators. Finally, we mounted the last home-made slave laser that was needed for the optical power amplification of the system, and we prepared the FPC setup on which the injection lock stability will be monitored in the future. These steps are essential for cooling and trapping the strontium atoms that will be used in the new experiment.

Regarding its present status, the vacuum system and the structure for magnetic field control in the experiment have been recently assembled. The optical components for the cooling stages are being prepared, and once the injection of the slave lasers is achieved, we would be able to use the prepared laser system to cool down strontium atoms to the mK regime. After using the red transition for further cooling, the optical tweezers—for which a test setup has been developed [56]—will be loaded. With these first steps, the experimental sequence is planned to enable quantum simulations of LGTs in more than one spatial dimension, finally achieving this long-term goal of the scientific community.

60FC-SF-4-A4.5S-01; polarising beam splitters *Foctek, PBS5204 (H-ZF2)*; mirrors *Thorlabs, BB1-E02*; $\lambda/2$-plates *Foctek, WPL212H*; shutters *home-made*.

[10] This tool is based on a reflective holographic grating *Thorlabs GH13-24U*. The output of a single mode fiber is collimated by a first lens onto the grating, and a second lens focusses the diffracted light into a CCD camera. Lenses: *Thorlabs AC254-100-A*; camera: *FLIR CMLN-13S2M-CS*. [46, 55]

References

[1] R. P. Feynman, "Simulating physics with computers," *International Journal of Theoretical Physics*, vol. 21, no. 6, pp. 467–488, Jun. 1982.

[2] A. J. Daley, I. Bloch, C. Kokail, S. Flannigan, N. Pearson, M. Troyer, and P. Zoller, "Practical quantum advantage in quantum simulation," *Nature*, vol. 607, no. 7920, pp. 667–676, Jul. 2022.

[3] I. Bloch, J. Dalibard, and S. Nascimbène, "Quantum simulations with ultracold quantum gases," *Nature Physics*, vol. 8, no. 4, pp. 267–276, Apr. 2012.

[4] C. Gross and I. Bloch, "Quantum simulations with ultracold atoms in optical lattices," *Science*, vol. 357, no. 6355, pp. 995–1001, Sep. 2017.

[5] A. Browaeys and T. Lahaye, "Many-Body Physics with Individually-Controlled Rydberg Atoms," *Nature Physics*, vol. 16, no. 2, pp. 132–142, Feb. 2020.

[6] R. Blatt and C. F. Roos, "Quantum simulations with trapped ions," *Nature Physics*, vol. 8, no. 4, pp. 277–284, Apr. 2012.

[7] T. Langen, G. Valtolina, D. Wang, and J. Ye, "Quantum state manipulation and cooling of ultracold molecules," *Nature Physics*, vol. 20, no. 5, pp. 702–712, May 2024.

[8] A. A. Houck, H. E. Türeci, and J. Koch, "On-chip quantum simulation with superconducting circuits," *Nature Physics*, vol. 8, no. 4, pp. 292–299, Apr. 2012.

[9] T. Hensgens, T. Fujita, L. Janssen, X. Li, C. J. Van Diepen, C. Reichl, W. Wegscheider, S. Das Sarma, and L. M. K. Vandersypen, "Quantum simulation of a Fermi–Hubbard model using a semiconductor quantum dot array," *Nature*, vol. 548, no. 7665, pp. 70–73, Aug. 2017.

[10] A. Aspuru-Guzik and P. Walther, "Photonic quantum simulators," *Nature Physics*, vol. 8, no. 4, pp. 285–291, Apr. 2012.

[11] M. H. Anderson, J. R. Ensher, M. R. Matthews, C. Wieman, and E. Cornell, "Observation of Bose-Einstein condensation in a dilute atomic vapor," *Science*, vol. 269, no. 5221, pp. 198–201, 1995.

[12] B. DeMarco and D. S. Jin, "Onset of Fermi degeneracy in a trapped atomic gas," *Science*, vol. 285, no. 5434, pp. 1703–1706, 1999.

[13] C. Chin, R. Grimm, P. Julienne, and E. Tiesinga, "Feshbach resonances in ultracold gases," *Reviews of Modern Physics*, vol. 82, no. 2, pp. 1225–1286, Apr. 2010.

[14] S. Kuhr, "Quantum-gas microscopes: a new tool for cold-atom quantum simulators," *National Science Review*, vol. 3, no. 2, pp. 170–172, Jun. 2016.

[15] D. Barredo, V. Lienhard, S. De Léséleuc, T. Lahaye, and A. Browaeys, "Synthetic three-dimensional atomic structures assembled atom by atom," *Nature*, vol. 561, no. 7721, pp. 79–82, Sep. 2018.

[16] S. Weinberg, *The Quantum Theory of Fields*. Cambridge University Press, 1996.

[17] M. C. Bañuls, R. Blatt, J. Catani, A. Celi, J. I. Cirac, M. Dalmonte, L. Fallani, K. Jansen, M. Lewenstein, S. Montangero, C. A. Muschik, B. Reznik, E. Rico, L. Tagliacozzo, K. Van Acoleyen, F. Verstraete, U.-J. Wiese, M. Wingate, J. Zakrzewski, and P. Zoller, "Simulating Lattice Gauge Theories within Quantum Technologies," *The European Physical Journal D*, vol. 74, no. 8, p. 165, Aug. 2020.

[18] T.-P. Cheng and L.-F. Li, *Gauge Theory of Elementary Particle Physics*. Oxford University Press, 1984.

[19] T. Senthil and M. P. A. Fisher, "$\mathbb{Z}_2$ Gauge Theory of Electron Fractionalization in Strongly Correlated Systems," *Physical Review B*, vol. 62, no. 12, pp. 7850–7881, Sep. 2000.

[20] G. Baskaran and P. W. Anderson, "Gauge theory of high-temperature superconductors and strongly correlated Fermi systems," *Phys. Rev. B*, vol. 37, pp. 580–583, Jan 1988.

[21] A. Lopez and E. Fradkin, "Fractional quantum Hall effect and Chern-Simons gauge theories," *Phys. Rev. B*, vol. 44, pp. 5246–5262, Sep 1991.

[22] C. Broholm, R. J. Cava, S. A. Kivelson, D. G. Nocera, M. R. Norman, and T. Senthil, "Quantum spin liquids," *Science*, vol. 367, no. 6475, p. eaay0668, 2020.

[23] E. A. Martinez, C. A. Muschik, P. Schindler, D. Nigg, A. Erhard, M. Heyl, P. Hauke, M. Dalmonte, T. Monz, P. Zoller, and R. Blatt, "Real-time dynamics of lattice gauge theories with a few-qubit quantum computer," *Nature*, vol. 534, no. 7608, pp. 516–519, Jun. 2016.

[24] C. Kokail, C. Maier, R. van Bijnen, T. Brydges, M. K. Joshi, P. Jurcevic, C. A. Muschik, P. Silvi, R. Blatt, C. F. Roos, and P. Zoller, "Self-Verifying Variational Quantum Simulation of the Lattice Schwinger Model," *Nature*, vol. 569, no. 7756, pp. 355–360, may 2019.

[25] N. H. Nguyen, M. C. Tran, Y. Zhu, A. M. Green, C. H. Alderete, Z. Davoudi, and N. M. Linke, "Digital quantum simulation of the schwinger model and symmetry protection with trapped ions," *PRX Quantum*, vol. 3, p. 020324, May 2022.

[26] H. Bernien, S. Schwartz, A. Keesling, H. Levine, A. Omran, H. Pichler, S. Choi, A. S. Zibrov, M. Endres, M. Greiner, V. Vuletić, and M. D. Lukin, "Probing many-body dynamics on a 51-atom quantum simulator," *Nature*, vol. 551, no. 7682, pp. 579–584, Nov. 2017.

[27] F. M. Surace, P. P. Mazza, G. Giudici, A. Lerose, A. Gambassi, and M. Dalmonte, "Lattice Gauge Theories and String Dynamics in Rydberg Atom Quantum Simulators," *Physical Review X*, vol. 10, no. 2, p. 021041, May 2020.

[28] B. Yang, H. Sun, R. Ott, H.-Y. Wang, T. V. Zache, J. C. Halimeh, Z.-S. Yuan, P. Hauke, and J.-W. Pan, "Observation of gauge invariance in a 71-site Bose–Hubbard quantum simulator," *Nature*, vol. 587, no. 7834, pp. 392–396, Nov. 2020.

[29] Z.-Y. Zhou, G.-X. Su, J. C. Halimeh, R. Ott, H. Sun, P. Hauke, B. Yang, Z.-S. Yuan, J. Berges, and J.-W. Pan, "Thermalization dynamics of a gauge theory on a quantum simulator," *Science*, vol. 377, no. 6603, pp. 311–314, Jul. 2022.

[30] A. Frölian, C. S. Chisholm, E. Neri, C. R. Cabrera, R. Ramos, A. Celi, and L. Tarruell, "Realizing a 1D topological gauge theory in an optically dressed BEC," *Nature*, vol. 608, no. 7922, pp. 293–297, Aug. 2022.

[31] C. Schweizer, F. Grusdt, M. Berngruber, L. Barbiero, E. Demler, N. Goldman, I. Bloch, and M. Aidelsburger, "Floquet approach to $\mathbb{Z}_2$ lattice gauge theories with ultracold atoms in optical lattices," *Nature Physics*, vol. 15, no. 11, pp. 1168–1173, Nov. 2019.

[32] A. Mil, T. V. Zache, A. Hegde, A. Xia, R. P. Bhatt, M. K. Oberthaler, P. Hauke, J. Berges, and F. Jendrzejewski, "A scalable realization of local U(1) gauge invariance in cold atomic mixtures," *Science*, vol. 367, no. 6482, pp. 1128–1130, Mar. 2020.

[33] C. J. Foot, *Atomic physics*. Oxford University Press, 2005.

[34] A. Celi, B. Vermersch, O. Viyuela, H. Pichler, M. D. Lukin, and P. Zoller, "Emerging Two-Dimensional Gauge Theories in Rydberg Configurable Arrays," *Physical Review X*, vol. 10, no. 2, p. 021057, Jun. 2020.

[35] J. Bergmann, "Simulation of lattice gauge theories with Rydberg atom arrays," PhD thesis proposal, Universitat Autònoma de Barceleona (UAB) - Institut de Ciències Fotòniques (ICFO), 2023.

[36] F. B. Dunning, T. C. Killian, S. Yoshida, and J. Burgdörfer, "Recent advances in Rydberg physics using alkaline-earth atoms," *Journal of Physics B: Atomic, Molecular and Optical Physics*, vol. 49, no. 11, p. 112003, Jun. 2016.

[37] I. S. Madjarov, J. P. Covey, A. L. Shaw, J. Choi, A. Kale, A. Cooper, H. Pichler, V. Schkolnik, J. R. Williams, and M. Endres, "High-Fidelity Entanglement and Detection of Alkaline-Earth Rydberg Atoms," *Nature Physics*, vol. 16, no. 8, pp. 857–861, Aug. 2020.

[38] M. Barbiero, "Novel techniques for a Strontium Optical Lattice Clock," PhD thesis, Politecnico di Torino, Mar. 2023.

[39] J. Höschele, "A strontium quantum-gas microscope," PhD thesis, Universitat Politècnica de Catalunya (UPC) - Institut de Ciències Fotòniques (ICFO), Mar. 2024.

[40] S. Stellmer, "Degenerate quantum gases of strontium," PhD thesis, University of Innsbruck, Faculty of Mathematics, Computer Science and Physics, Jan. 2013.

[41] R. Santra, K. V. Christ, and C. H. Greene, "Properties of metastable alkaline-earth-metal atoms calculated using an accurate effective core potential," *Physical Review A*, vol. 69, no. 4, p. 042510, Apr. 2004.

[42] I. Nosske, L. Couturier, F. Hu, C. Tan, C. Qiao, J. Blume, Y. H. Jiang, P. Chen, and M. Weidemüller, "Two-dimensional magneto-optical trap as a source for cold strontium atoms," *Physical Review A*, vol. 97, no. 3, p. 039901, Mar. 2018, arXiv:1709.00790 [cond-mat, physics:physics].

[43] S. Buob, J. Höschele, V. Makhalov, A. Rubio-Abadal, and L. Tarruell, "A Strontium Quantum-Gas Microscope," *PRX Quantum*, vol. 5, no. 2, p. 020316, Apr. 2024.

[44] R. Paschotta, "Injection locking," available online at https://www.rp-photonics.com/injection_locking.html.

[45] C. Gas-Ferrer, "Characterization and transverse laser cooling of a strontium atomic source," MSc thesis, Universitat Politècnica de Catalunya (UPC) - Institut de Ciències Fotòniques (ICFO).

[46] D. Jacobs, "Design and construction of a new experimental apparatus for the laser cooling of strontium," MSc thesis, Universität Hamburg - Institut de Ciències Fotòniques (ICFO), 2019.

[47] I. Manai, A. Molineri, C. Fréjaville, C. Duval, P. Bataille, R. Journet, F. Wiotte, B. Laburthe-Tolra, E. Maréchal, M. Cheneau, and M. Robert-de Saint-Vincent, "Shelving spectroscopy of the strontium intercombination line," *Journal of Physics B: Atomic, Molecular and Optical Physics*, vol. 53, no. 8, p. 085005, Apr. 2020.

[48] I. Prieto-Rodríguez, "Doppler-free spectroscopy of strontium atoms on the 461 nm transition," Internship report, Universitat de Barcelona (UB) - Institut de Ciències Fotòniques (ICFO), Barcelona, June 2024.

[49] D. Sun, C. Zhou, L. Zhou, J. Wang, and M. Zhan, "Modulation transfer spectroscopy in a lithium atomic vapor cell," *Optics Express*, vol. 24, no. 10, p. 10649, May 2016.

[50] J. H. Shirley, "Modulation transfer processes in optical heterodyne saturation spectroscopy," *Optics Letters*, vol. 7, no. 11, p. 537, Nov. 1982.

[51] L. Mudarikwa, K. Pahwa, and J. Goldwin, "Sub-Doppler modulation spectroscopy of potassium for laser stabilization," *Journal of Physics B: Atomic, Molecular and Optical Physics*, vol. 45, no. 6, p. 065002, Mar. 2012.

[52] M. Landini, "A tunable Bose-Einstein condensate for quantum interferometry," PhD thesis, Università degli Studi di Trento, 2011.

[53] D. J. McCarron, S. A. King, and S. L. Cornish, "Modulation transfer spectroscopy in atomic rubidium," *Measurement Science and Technology*, vol. 19, no. 10, p. 105601, Oct. 2008.

[54] G. Ellis, *Control System Design Guide.* Elsevier Academic Press, 2004.

[55] J. D. White and R. E. Scholten, "Compact diffraction grating laser wavemeter with subpicometer accuracy and picowatt sensitivity using a webcam imaging sensor," *Review of Scientific Instruments*, vol. 83, no. 11, p. 113104, Nov. 2012.

[56] T. Dardier, "An optical tweezeres setup for a new Rydberg atom array experiment to quantum simulate lattice gauge theories," Internship report, École Normale Supérieure Paris-Saclay, Institut de Ciències Fotòniques (ICFO), Barcelona, June 2024.

[57] Moglabs, *External Cavity Diode Laser LDL Littrow Enhanced.*

[58] J. Moore, C. Davis, and M. Coplan, *Building Scientific Apparatus.* Cambridge University Press, 2009.

[59] K. Iga, Ed., *Encyclopedic handbook of integrated optics.* Boca Raton: CRC, 2006.

[60] T. Schneider, *Nonlinear Optics in Telecommunications.* Springer Berlin Heidelberg, 2004.

[61] G. Camy, C. Bordé, and M. Ducloy, "Heterodyne saturation spectroscopy through frequency modulation of the saturating beam," *Optics Communications*, vol. 41, no. 5, pp. 325–330, May 1982.

[62] R. Paschotta, "Acousto-optic modulators," available online at https://www.rp-photonics.com/acousto_optic_modulators.html.

[63] W. Klein and B. Cook, "Unified approach to ultrasonic light diffraction," *IEEE Transactions on Sonics and Ultrasonics*, vol. 14, no. 3, pp. 123–134, 1967.

[64] M. Duocastella, S. Surdo, A. Zunino, A. Diaspro, and P. Saggau, "Acousto-optic systems for advanced microscopy," *Journal of Physics: Photonics*, vol. 3, no. 1, p. 012004, nov 2020.

[65] E. A. Donley, T. P. Heavner, F. Levi, M. O. Tataw, and S. R. Jefferts, "Double-pass acousto-optic modulator system," *Review of Scientific Instruments*, vol. 76, no. 6, p. 063112, Jun. 2005.

A Lab pictures

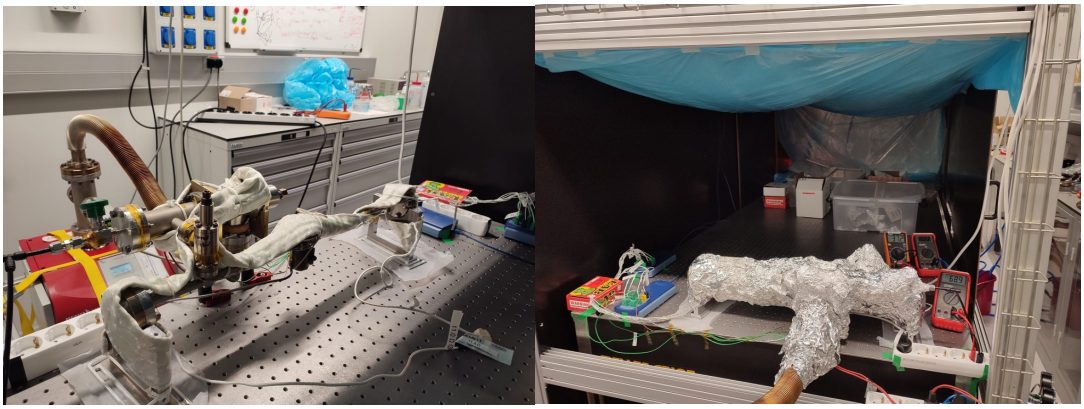

Figure 16: Heat pipe bake out: main band heater (left) and aluminium covering (right).

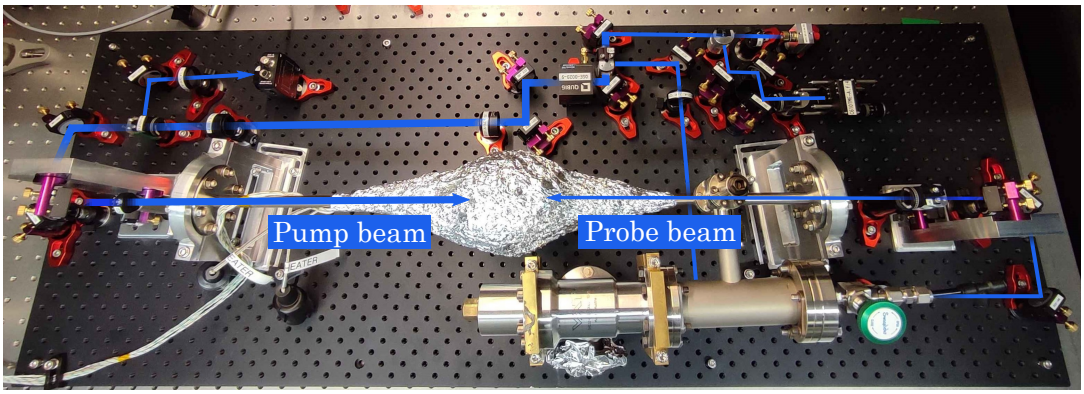

Figure 17: Spectroscopy setup.

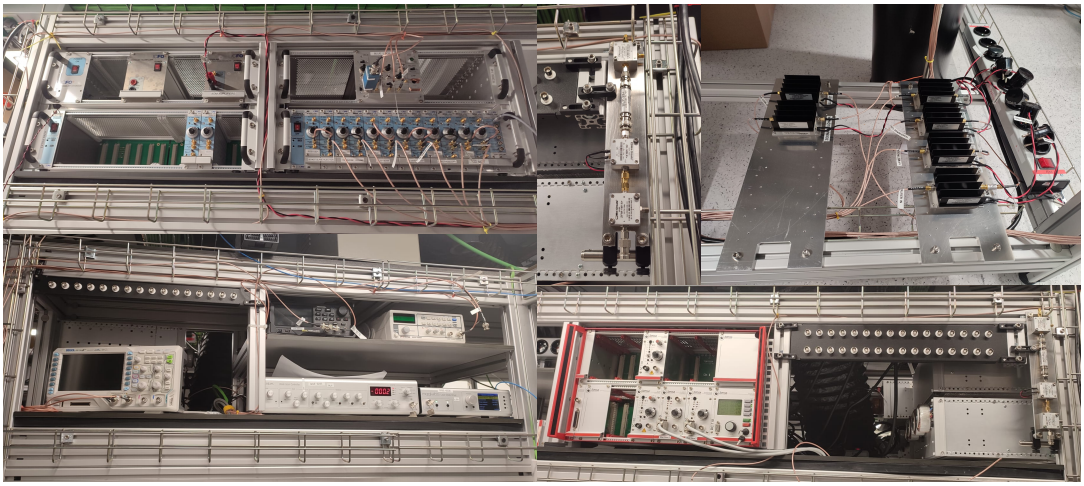

Figure 18: Electronics organisation in the lab.

Figure 19: Laser system setup.

B Littrow configuration of an ECDL

The commercial master laser[11] that we use is an external cavity diode laser (ECDL) in the Littrow configuration. It is based on a semiconductor laser diode accompanied by a tunable diffraction grating, both of which form a cavity that allows for wavelength control. This cavity is referred to as *external* cavity, as opposed to the *internal* cavity formed by the two facets of the laser diode. In the Littrow configuration, the diode light is collimated and diffracted by the adjustable grating. The first order diffracted beam is sent back to the laser diode as an optical feedback whose central wavelength is given by

$$\lambda = 2d \sin\theta, \tag{16}$$

where d is the grating spacing and θ is the incident angle with respect to the grating normal. The schematics of the ECDL Moglabs laser is depicted in Fig. 20. A fold mirror is used to make the output beam parallel to the input beam generated by the diode. This mirror and the tunable grating are mounted on a rotating puck whose orientation can be adjusted with a screw, allowing for the coarse variation of the wavelength without modifying the output beam direction. A piezo-electric transducer acting on the grating and thus controlling the external cavity length is used for fine tuning of the wavelength λ.

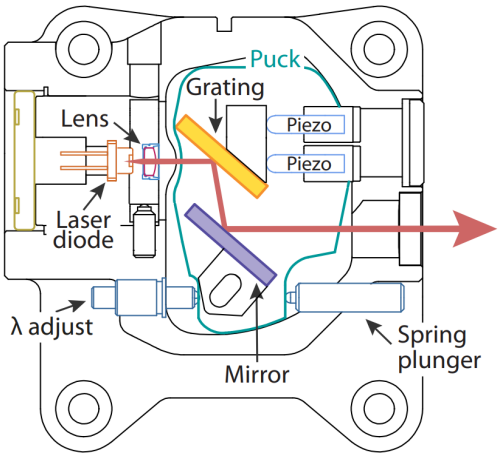

Figure 20: Schematics of the ECDL of the Moglabs master laser. This figure is obtained from Ref. [57].

The laser wavelength is also affected by the diode current and cavity temperature. The latter is internally sensed with a thermistor, and adjusted to the set value with a Peltier thermoelectric cooler (TEC), similarly to what we plan to do on the home-made slave lasers of these project.

[11] Moglabs, ILA-A52103016

C Bake out of the heat pipe

In this appendix, the attainment of high vacuum in the heat pipe for spectroscopy is described.

The out-gassing of impurities from the inner walls of our apparatus is the major limiting factor for reaching the high vacuum regime. To overcome this, a *bake out* procedure was followed. It consists of heating the system in order to enhance the associated desorption rate, and remove the liberated compounds with a pumping system [58]. Thus, the heat pipe was connected to a bellow joined to a turbo-molecular pump[12] through the CF40 valve designed to that end, and the temperature of the whole apparatus was increased using heating tapes[13] and a collar heater[14], each connected to a variable transformer[15] which was used to control the heating rate. In order to prevent the viewports from being damaged during this process, they were previously replaced by blank flanges. Several thermocouples[16] were attached to the heat pipe to monitor the temperature at different points, and the pressure was measured by a vacuum gauge[17] in the turbo pump. The whole structure was wrapped in aluminum foil to enhance the thermal homogeneity, and to isolate the system from the environment. Quick temperature changes can lead to severe problems in the vacuum valves. They are composed of different kinds of metals, whose thermal expansion coefficients differ, and a rapid temperature variation would cause irreversible deformations, opening leaks that would be impossible to fix without replacing these pieces. To guarantee the safety of the valves in the system, the temperature was increased at a rate below 10 °C/h.

Panels (b) and (c) in Fig. 21 show the temporal evolution of the temperature—measured by the sensor at the hottest spot—and the pressure of the heat pipe during bake out. The relation of this two variables is displayed in panel (a) on the same figure, where we plot the pressure vs. the inverse of the temperature. The color code shows the temporal evolution. The effectiveness of the bake out procedure can be deduced from this graph: at the same temperatures, we observe that the pressure values while heating up the system (red) are higher than those corresponding to the temperature decrease (blue), after removing most of the compounds adsorpted to apparatus. Naturally, the overall final pressure is lower than the initial one, although the sensitivity of our pressure sensor in this low range (10^{-9} mbar) yields a rather subtle measured difference: the initial pressure was approximately 4×10^{-9} mbar, and the final value was 2×10^{-9} mbar.[18]

The pressure P evolution in the above-described desorption process follows an Arrhenius-type equation,

$$P = P_0 \, e^{-\frac{E_a}{RT}}, \tag{17}$$

where P_0 is a pressure constant, E_a is the activation energy of the adsorption of gases

[12] Pfeiffer Vacuum Hicube 80 Classic Turpo Pump Station

[13] Omegalux SWH251-060, SRHT-050X24-240

[14] Watlow St. Louis, MB2A1JN1-B12

[15] RS Pro 1 Phase 720VA Variac, 1 Output, 240V (890-2803), RS Pro 1 Phase 480VA Variac, 1 Output, 240V (890-2793).

[16] RS PRO thermocouples types K and J

[17] Agilent UHV-24P ION GAUGE,2 THOR/IRIDM, 2.75

[18] Moreover, a previous bake out was started, but it ended abruptly due to a shortcut in a damaged band heater. Even though it could not be successfully completed, this initial bake out seems to have been quite effective, allowing us to decrease the vacuum pressure at room temperature from 2×10^{-7} mbar to 4×10^{-9} mbar. Therefore, most of the adsorpted gases and impurities were already removed in this first "frustrated" baking.

and impurities on the inner walls of the pipe, R denotes the ideal gas constant, and T is the temperature. Therefore, it is possible to extract the value of E_a by doing a linear fit of $\log(P)$ vs. $1/T$ in the high-temperature range for the data corresponding to cooling, when this phenomenon occurs. The experimental data and this fit are displayed in Fig. 21. The resulting value of the activation energy is $E_a = (27.4 \pm 0.3)$ kJ/mol, where the error corresponds to a 68% confidence interval.

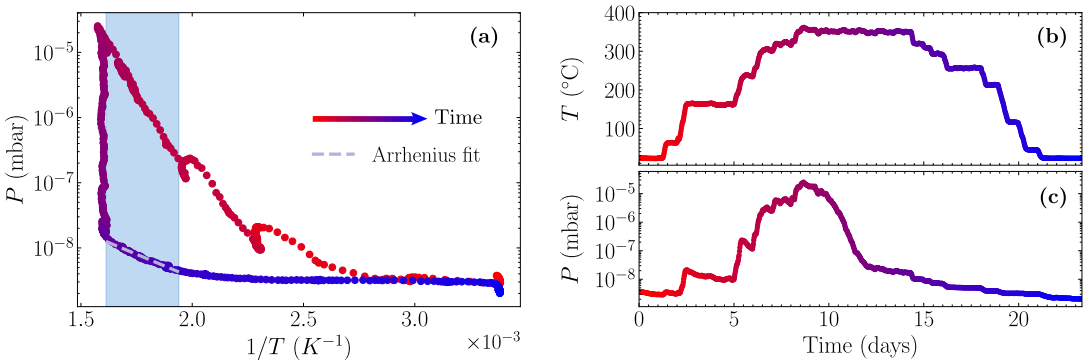

Figure 21: Bake out process. **(a)** Pressure (in logarithmic scale) vs. the inverse of the temperature during bake out. The curve follows the Arrhenius scaling in the highlighted region employed for the fit (dashed grey line), in which the coefficient of determination is $R^2 = 0.99$. We observe some pressure decrements on the heating curve, which correspond to some plateaus in the temporal evolution of the temperature—shown on panel **(a)**—. When the temperature was kept constant, the pressure was still reduced by the turbo pump, as we see more abruptly on the vertical purple segment on the left plot. Panel **(c)** shows the temporal evolution of the pressure during bake out, also in logarithmic scale.

After bake out, the viewports were inserted again. We performed a leak test based on monitoring pressure changes while spraying helium on the joints. Helium is the smallest non-reactive atom, and it would get inside the heat pipe if there was a leak. Our vacuum gauge is less sensitive to helium compared to other gases, so the measured pressure value decreases if helium gets inside the apparatus. This allowed us to do multiple leak tests, and guarantee a good level of high vacuum. The detected leaks were fixed by re-tightening the necessary screws.

Then, we introduced 25 g of 99.99% purified strontium[19] in the heat pipe chamber, and a helium leak test was performed again. Afterwards, argon at approximately 10^{-3} mbar was introduced in the heat pipe as a buffer gas. For the sake of avoiding large vertical temperature gradients in the future, we placed a second collar heater[20] around the top part of the central chamber of the heat pipe, in addition to the initial collar heater around the reservoir. Finally, the system was covered by several layers of thermally isolating fiber glass and aluminum foil. The heat pipe was disconnected from the turbo pump after measuring the first spectroscopy signal, and ensuring that the amount of argon introduced was adequate to obtain an appropriate signal while ensuring the protection of the viewports. Inserting too much argon would yield an excessive collisional broadening, reducing the frequency sensitivity for the spectroscopy lock.

[19] Sigma-Aldrich, 441899

[20] Watlow St. Louis, MB2A1N1-B12, 240 V 350 W 1919

D MTS working principles: four wave mixing and heterodyne detection

Four wave mixing

In the electro optic modulator which we use, the refractive index of a MgO:$LiNbO_3$ (MLN) crystal is modulated by an applied driving voltage. The phase of the outgoing light beam is directly proportional to the traveled optical path, defined as $\mathcal{L} \equiv \int n(\vec{r})\, dl$, where $n(\vec{r})$ is the refractive index of the medium as a function of the position, and dl is the differential element of the path length. Therefore, the driving voltage produces a phase modulation in the light field, which can be expressed as

$$\begin{aligned} E(t) =& E_0 \sin\left[\omega t + \phi_0 \sin(\omega_m t)\right] \\ =& E_0 \left\{ \sum_{n=0}^{\infty} J_n(\phi_0) \sin\left[(\omega + n\omega_m)t\right] + \sum_{n=1}^{\infty} (-1)^n J_n(\phi_0) \sin\left[(\omega - n\omega_m)t\right] \right\}, \end{aligned} \tag{18}$$

where $J_n(\phi_0)$ is the Bessel function of order n evaluated at ϕ_0, ω_m is the modulation frequency, and ω is the carrier frequency. Generally, $\phi_0 \ll 1$, so we can approximate Eq. (18) as follows,

$$E(t) \simeq E_0 \left\{ \sin(\omega)t + J_1(\phi_0) \left[\sin(\omega_+ t) - \sin(\omega_- t) \right] \right\}, \tag{19}$$

where $\omega_\pm \equiv \omega \pm \omega_m$. Thus, the modulated pump beam can be described as a carrier wave with $(\omega, \vec{k})$ and two sidebands with $(\omega_\pm, \vec{k}_\pm)$. They propagate, altogether with the probe beam, characterised by $(\omega, -\vec{k})$, through the atomic vapour, which is a non-linear medium. This generates a phase modulation in the probe beam by means of *four wave mixing* [**?**, 59, 60], an effect arising from the propagation of different frequency components in a nonlinear medium. This generates a phase modulation in the probe beam by means of a non-linear effect known as *four wave mixing*. This underlying physical phenomenon is associated with the propagation of three waves with at least two different frequencies in a non-linear medium, in which a new frequency component in the polarisation third-order non-linearity emerges,

$$P_{\mathrm{NL}} = \frac{1}{2} \chi^{(3)} A_1 A_2 A_3^* e^{i\left[(\omega_1 + \omega_2 - \omega_3)t - \left(\vec{k}_1 + \vec{k}_2 - \vec{k}_3\right)\cdot \vec{r}\right]}, \tag{20}$$

where $(A_j, \omega_j, \vec{k}_j)$, with $j = 1, 2, 3$, are the complex amplitude, frequency, and wavevector of each wave, and $\chi^{(3)}$ is the third-order susceptibility of the medium. This non-linear polarisation generates a fourth light wave whose frequency and wavevector are $(\omega_4, \vec{k}_4)$. The conservation of photon energies and momenta (or, equivalently, the phase matching condition) imply that

$$\omega_1 + \omega_2 = \omega_3 + \omega_4, \quad \vec{k}_1 + \vec{k}_2 = \vec{k}_3 + \vec{k}_4. \tag{21}$$

The pump carrier, the probe beam, and each of the pump sidebands interact in this manner, with $\omega_1 = \omega_2 = \omega$, $\omega_3 = \omega_\pm$; $\vec{k}_1 = -\vec{k}_2 = \vec{k}$, $\vec{k}_3 = \vec{k}_\pm$ [53]. We talk about *degenerate* four wave mixing because two of the interacting waves have the same frequency. This process generates two sidebands for the probe beam, with $\omega_4 = \omega_\mp$, and $\vec{k}_4 = -\vec{k}_\pm$, transmitting the phase modulation to it. Finally, the probe light is collected in a photodetector.

Heterodyne detection

The transferred modulation can be measured heterodyne detection. This allows for the obtention of an error signal which is proportional to the original spectral feature, as we

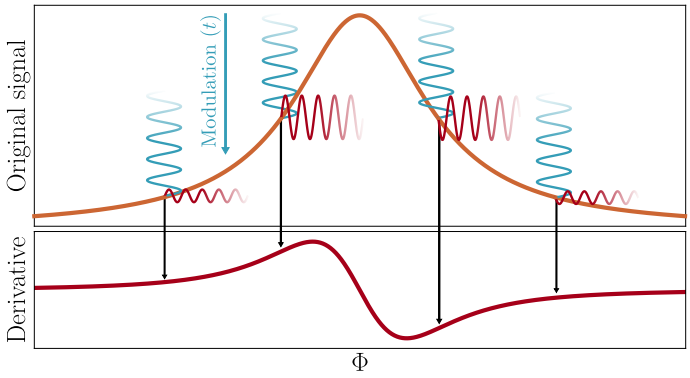

Figure 22: The transferred phase modulation in the probe light field and the subsequent demodulation through heterodyne detection leads to an error signal which is proportional to the original one.

explain in the following. The phase of the probe light field at the photodetector, taking into account the transferred modulation, can be approximately written as

$$\Phi(t) \equiv \Phi_0(t) + \xi \sin(\omega_m t), \tag{22}$$

where $\Phi_0(t) \equiv \omega t$ is the unmodulated phase, and ξ is the amplitude of the transferred modulation. The photodetector signal can be approximated as

$$S(\Phi) \equiv S(\Phi_0) + \left.\frac{dS}{d\Phi}\right|_{\Phi=\Phi_0} \xi \sin(\omega_m t). \tag{23}$$

In heterodyne detection, this signal is mixed with the driving modulation,

$$\begin{aligned} S(\Phi) \times \sin(\omega_m t) &= \left[S(\Phi_0) + \xi \sin(\omega_m t) \left.\frac{dS}{d\Phi}\right|_{\Phi=\Phi_0}\right] \times \sin(\omega_m t) \\ &= S(\Phi_0)\sin(\omega_m t) + \frac{\xi}{2}\Big[1 - \cos(2\omega_m t)\Big] \left.\frac{dS}{d\Phi}\right|_{\Phi=\Phi_0}. \end{aligned} \tag{24}$$

Then, the signal at the output of the frequency mixer is sent to a low pass filter (LPF) which filters out the high frequency components in Eq. 24, yielding an error signal proportional to the derivative of the input, $dS/d\Phi|_{\Phi=\Phi_0}$. This is illustrated in Fig. 22.

In the preceding analysis in which we obtained Eq. 24, we referred to the derivative of the spectral feature with respect to the phase. Nevertheless, the phase is linearly related to the detuning δ, so the derivative with respect to δ can be equivalently considered—as we do in the main text for the sake of clarity.

Note that heterodyne detection also serves for saturation spectroscopy with frequency (instead of phase, as in our case) modulation of the pump beam, as explained in Ref. [61].

E AOMs: fundamentals and double-pass configuration

AOMs are formed by a transparent crystal (in our case, made of TeO_2) attached to a piezo electric transducer, which is driven by an RF signal. This generates a longitudinal[21] sound wave propagating through the crystal, which induces a periodic change in its refractive index due to the photoelastic effect. This periodic variation produces a diffraction grating, in which the frequency shift between successive diffraction orders is fixed by the sound wave frequency [62]. In general, an acousto-optical device can operate in two distinct regimes depending on the effective thickness of the vibrating medium and the angle of incidence of the incoming light. The first property is quantified by a parameter defined by Klein and Cook [63],

$$Q \equiv \frac{2\pi\lambda L f_m^2}{n_0 v^2}, \tag{25}$$

where λ is the laser light, f_m is the acoustic frequency, and L, n_0, v are, respectively, the thickness, static refractive index, and sound velocity of the crystal.

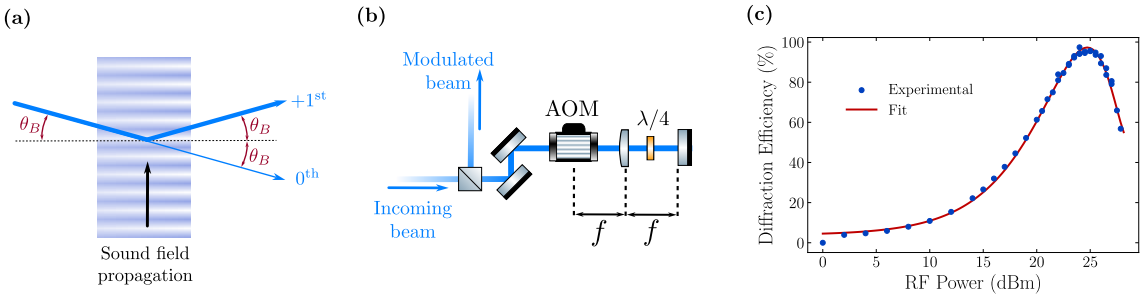

Figure 23: AOM characterisation. **(a)** Geometrical illustration of the working principle. **(b)** Double-pass AOM setup and double-pass configuration. The distance f denotes the focal distance of the lens composing the cat's eye retroreflector. **(c)** Diffraction efficiency vs. RF power. Blue points correspond to experimental data, and the red solid line gives a polynomial fit.

A device operates in the *Raman-Nath* regime when $Q \ll 1$ and the light beam enters the sound field at normal incidence. The generated diffraction pattern includes many orders, for which the diffraction efficiency (defined as the fraction of the incident light intensity) is limited to approximately 34% [64]. Nevertheless, AOMs operate in the so-called *Bragg* regime, for which $Q \gg 1$ and the laser beam enters the device at the Bragg angle θ_B, given by the following relation,

$$\sin\theta_B = \frac{\lambda f_m}{2n_0 v}. \tag{26}$$

When the Bragg condition is verified, there is approximately a single diffraction order ($\pm 1^{st}$, depending on the sign of the incident angle), which takes most of the incident intensity ($\geq 60\%$). In addition, the diffracted beam is deflected by the same angle θ_B (see Fig. 23a). This deflection incorporates the possibility of using the AOM as an electric switch, much faster than a mechanical shutter. However, the deflection of the outgoing beam also hinders the possibility of scanning the modulation frequency f_m, since the Bragg angle depends of it. One common approach for overcoming this problem is to use a double-pass configuration [65]. Therein, the laser beam travels through the AOM twice and the beam deflection is therefore compensated. However, this involves a reduction of the AOM efficiency, which becomes the square of the single-pass value. Therefore, for applications in which reducing the light power losses is crucial, it is more convenient to use single-pass

[21] In other acousto-optical devices, such as acousto-optical deflectors (AODs), the sound wave is transversal.

AOMs, although this implies that the alignment of the setup will only allow for a fixed modulation frequency.

Panel (b) on Fig. 23 shows a schematic of each AOMs setup. In the case of the double pass AOMs, they are followed by a so-called *cat's eye retroreflector*, which consist of a lens and a mirror with a spacing equal to the focal length of the lens. Specifically, in our layout the distance between the AOM and the lens is also equal to this focal length. In this manner, although the diffraction angle is changed as the modulating frequency is swept, the diffracted beam always emanates from the focal point of the lens, after which it is parallel to the 0^{th} order beam. Afterwards, the mirror is aligned so that the diffracted beam arrives to it at normal incidence. In order to separate the input and output beams, we use a polarising beam splitter and a QWP, as it is shown in Fig. 23.

The single-pass diffraction efficiency of one of our AOMs as a function of the RF driving power is plotted on panel (c) in Fig. 23.